1 **Machine Learning Assisted Chemical Characterization and Optical Properties of**

2 **Atmospheric Brown Carbon in Nanjing, China**

3 Yu Huang[1], Xingru Li[2], Dan Dan Huang[3], Ruoyuan Lei[1], Binhuang Zhou[1],

4 Yunjiang Zhang[1], Xinlei Ge[1, 4*]

5

6 [1] Jiangsu Key Laboratory of Atmospheric Environment Monitoring and Pollution

7 Control, Collaborative Innovation Center of Atmospheric Environment and Equipment

8 Technology, School of Environmental Science and Engineering, Nanjing University of

9 Information Science and Technology, Nanjing 210044, China

10 [2] Analytical Instrumentation Center, Department of Chemistry, Capital Normal

11 University, Beijing, 100048, China

12 [3] Shanghai Academy of Environmental Sciences, Shanghai 200233, China

13 [4] School of Environment and Energy Engineering, Anhui Jianzhu University, Hefei

14 230601, China

15 *Corresponding author: Xinlei Ge (Email: caxinra@163.com)

16

17

18

Abstract: The light-absorbing organics, namely brown carbon (BrC), can significantly affect atmospheric visibility and radiative forcing, yet their chemical and optical properties remain poorly understood. Here, a comprehensive analysis was conducted on the particulate matter ($PM_{2.5}$) samples collected in Nanjing, China during 2022 ~ 2023 with a particular interest on the identification of key BrC molecules. First, the water-soluble organic aerosol (WSOA) was more oxygenated during cold season (CS) due to a highly oxidized secondary OA (SOA) factor that was strongly associated with aqueous/heterogeneous reactions especially during nighttime, while the WSOA during summer season (SS) was less oxygenated and the SOA was mainly from photochemical reactions. Fossil fuel combustion hydrocarbon-like OA was the largest and dominant contributor to the light absorption during CS (55.6 ~ 63.7%). Secondly, our observations reveals that aqueous oxidation can lead to notable photo-enhancement during CS, while photochemical oxidation on the contrary caused photo-bleaching during SS; Both water-soluble and methanol-soluble organics had four key fluorophores, including three factors relevant with humic-like substances (HULIS) and one protein-like component. Thirdly, molecular characterization show that CHON compounds were overall the most abundant species, followed by CHO and CHN compounds, and significant presence of organosulfates in CS samples reaffirmed the importance of aqueous-phase formation. Finally, building upon the molecular characterization and light absorption measurement results, the machine learning approach was applied to identify the key BrC molecules, and 31 compounds including polycyclic aromatic hydrocarbons (PAHs), oxyheterocyclic PAHs, quinones, and nitrogen-containing species, etc., which can be a good reference for future studies.

1 Introduction

In ambient air, some organic aerosol (OA) species can absorb light in the near-ultraviolet (UV) and visible spectrum, and are termed as brown carbon (BrC) (Andreae and Gelencsér, 2006; Chen et al., 2020b). The BrC absorption exhibits strong wavelength-dependence that typically the absorption increases as the wavelength decreases (Laskin et al., 2015). A prior study has reported that BrC is responsible for approximately 40 % of UV-Vis light absorption (Yan et al., 2018), and thus BrC can play a crucial role in global climate and air quality (Jo et al., 2016; Feng et al., 2013). For examples, some studies show that the global radiative forcing of BrC ranges from approximately 0.22 to 0.57 W m^{-2}, equivalent to 27 ~ 70 % of that of black carbon (BC) (Lin et al., 2014; Zhang et al., 2017). Given such importance, recently many researches have been conducted to characterize the optical properties, sources, as well as chemical composition of BrC.

The sources of atmospheric BrC are highly complex, as it can originate from multiple primary emissions (Hecobian et al., 2010; Chakrabarty et al., 2010; Gu et al., 2022) as well as various secondary chemical processes (Wang et al., 2021) (Fleming et al., 2020; Jiang et al., 2021; Chen et al., 2020b). The primary sources mainly include coal combustion, biomass burning, and vehicular emissions (Wang et al., 2016; Sun et al., 2016; Qi et al., 2019; Chen et al., 2018; Gu et al., 2022); besides, a significant presence of chromophores originating from the ocean has been observed, indicating that the ocean/marine emission is likely also an important source of BrC (Cavalli et al., 2004). As said, secondary BrC species can be generated from many processes, for instances, the aromatic secondary OA (SOA) species formed under high NO$_x$ concentrations (Jaoui et al., 2006), reaction products of biogenic or anthropogenic SOAs with nitrogen-containing substances such as NH$_3$ and NH$_4^+$ (Updyke et al., 2012; Shapiro et al., 2009; Bones et al., 2010), and aqueous-phase reaction products from various carbonyl/phenolic precursors in cloud, fog, and aerosol water (Hu et al., 2017; Ye et al., 2018; Wang et al., 2021; Li et al., 2023; Ou et al., 2021). The light absorption properties of BrC are also closely related with its sources. Recent studies have linked

72   BrC light absorption with its various sources (both primary and secondary)

73   deconvoluted from factor analysis of OA data determined by the aerosol mass

74   spectrometry (AMS) (Chen et al., 2020b; Zhong et al., 2023; Chen et al., 2016), and

75   provided the mass absorption efficiency (MAE) of individual BrC source/factor. In

76   addition, the fluorescent properties are also investigated, which identified different

77   types of humic-like substances (HULIS) and protein-like species as the key components

78   (Xie et al., 2020; Chen et al., 2020a; Chen et al., 2021).

79   Essentially, the light absorption properties of BrC are governed by its chemical

80   constitution. Current studies have identified several key classes of light-absorbing

81   organics in atmospheric aerosols, such as the aromatic carboxylic acids, phenols,

82   nitroaromatic compounds (NACs), polycyclic aromatic hydrocarbons (PAHs) and their

83   derivatives (Lin et al., 2018; Huang et al., 2018; Wang et al., 2021; Xing et al., 2023;

84   Gu et al., 2022; Chen et al., 2020b; Kuang et al., 2023). Some lignin pyrolysis/burning

85   products including coumarins, flavonoids, stilbenes, and several sulfur-containing

86   species are also found as significant BrC constituents (Fleming et al., 2020;

87   Budisulistiorini et al., 2017; Huang et al., 2022). Xing et al. (2023) identified a series

88   of BrC chromophores, encompassing nitrophenols, benzoic acids, oxygenated PAHs,

89   phenols, aryl amides/amines, phenylpropene derivatives, coumarins and flavonoids,

90   pyridines, and nitrobenzoic acids. Nevertheless, knowledge regarding the molecular

91   composition of BrC so far is still incomplete and the aforementioned identified species

92   only occupy a limited fraction of the BrC total light absorption. For examples, Zhang

93   et al. (2013) measured eight NACs in Los Angeles and found that they contributed about

94   4 % of water-soluble BrC light absorption at 365 nm; Huang et al. (2018) measured 18

95   PAHs and their derivatives in Xi'an and found that they accounted for on average ∼ 1.7 %

96   of the overall absorption of methanol-soluble BrC; Gu et al. (2022) quantified eight

97   NACs present in $PM_{2.5}$ samples collected during winter in Nanjing, which together

98   could account for at most ∼9 % of the total BrC absorption at 365 nm.

99   Emerging non-targeted approaches based on gas chromatography (GC) or liquid

100   chromatography (LC) coupled with high-resolution mass spectrometry can detect

101 hundreds to thousands of molecules in OA (Kuang et al., 2023; Mao et al., 2022),

102 enabling the identification of potential BrC species by connecting them with light

103 absorption of OA. However, these approaches often output high-dimensional data with

104 numerous variables, which must be evaluated appropriately. Traditional statistical

105 methods often perform poorly when handling large datasets and fail to accurately

106 identify complex relationships between variables (Fasola et al., 2020). Machine

107 learning (ML) is a powerful tool that can effectively recognize nonlinear relationships

108 between variables and address issues of collinearity among them (Tang et al., 2024).

109 For instances, Zhang et al. (2023) employed the Random Forest (RF) algorithm to

110 quantify the factors driving $PM_{2.5}$ trends in six cities on Tibetan Plateau from 2015 to

111 2022, revealing the importance of anthropogenic emission reductions; Wang et al.

112 (2022a) integrated the positive matrix factorization (PMF) with a multi-layer

113 perceptron (MLP) neural network to analyze the sources of BrC light absorption in six

114 major Chinese cities, which finds that primary emissions, including biomass burning,

115 vehicle emissions, and coal combustion, significantly contribute to BrC in these cities,

116 while secondary processes contributed more significantly to light absorption in

117 southern cities than in northern cities.

118 In this study, we conducted a systematic investigation on the chemical and optical

119 properties on the fine particular matter ($PM_{2.5}$) samples in both daytime and nighttime

120 collected in Nanjing, China during summer and cold seasons of 2022 ~ 2023.

121 Particularly, for the first time, we applied the ML RF algorithm to connect the light-

122 absorbing characteristics with the determined organic molecular identities, to assist the

123 screen of key BrC molecules. Our findings regarding the BrC properties, and especially

124 the BrC molecules proposed here can be a good reference for future studies.

125

126 **2 Experimental methods**

127 **2.1 Sampling site and sample collection**

128 The $PM_{2.5}$ filter samples were collected in the Nanjing, China, from July 11 to

129 August 23, 2022, November 30 to December 10, 2022, February 13 to February 20,

130 2023, and March 3 to March 31, 2023. The first period represents the hot summer

131 season (SS) (81 samples), and the later three periods represent the cold season (CS)(83

132 samples); note samples were not collected during precipitation events in both seasons.

133 The sampling site was located inside the campus of Nanjing University of Information

134 Science and Technology (32°12'20.82"N, 118°42'25.46"E). The site was in a suburban

135 area, surrounded by residential buildings, and close to traffic arteries, and industrial

136 zones (including chemical engineering and petrochemical plants, power plants and

137 ironmaking and steelmaking plants).

138 A high volume sampler (Jinshida Ltd. Qingdao, China, model KB-1000) with a

139 flow rate of 1.05 m^3 min^{-1} was employed. $PM_{2.5}$ samples were collected on the prebaked

140 (450 °C) quartz fiber filters (Pallflex, USA, size of 8 × 10 inch). Daytime samples were

141 collected from 08:00 to 18:00 (Local Beijing time), and nighttime samples were

142 collected from 19:00 to 07:00 on the next day. Each filter was wrapped in an aluminum

143 foil and kept frozen at -20 °C until analysis. The concentrations of common gas

144 pollutants (SO_2, NO_2, CO, and O_3) were obtained from the nearby National

145 Environmental Monitoring Center (http://www.cnemc.cn/), while the meteorological

146 parameters (air temperature, relative humidity, wind speed and direction) were recorded

147 in the same site as $PM_{2.5}$.

148

149 **2.2 Chemical analyses**

150 **2.2.1 Measurements of inorganic ions, organic carbon (OC) and elemental**

151 **carbon (EC)**

152 A number of round pieces (20 mm diameter) were punched from each sample filter,

153 and were extracted by using 50 mL of ultrapure water (18.25 MΩ cm) (10 pieces) and

154 methanol (4 pieces), respectively. The filter pieces underwent 30 minutes of sonication

155 and were filtrated through the polytetrafluoroethylene (PTFE) syringe filters (0.22 μm)

156 to remove insoluble materials. Cations (NH_4^+, Na^+, K^+, Mg^{2+}, Ca^{2+}) were measured

157 using a 881 Compact IC pro ion chromatography (Metrohm, Switzerland), anions

158 (NO_3^-, SO_4^{2-}, Cl^-, F^-) are determined by the ICS2100 (Dionex, USA). The water-

159   soluble organic carbon (WSOC) (μg C m^{-3}) was measured by a total organic carbon

160   (TOC) analyzer (TOC-L, Shimazu, Japan). Operational details of these analyses can

161   be found in our previous work (Chen et al., 2020a).

162   Concentrations of total elemental carbon (EC) and organic carbon (OC) in samples

163   were measured using a thermal optical carbon analyzer (RT-4; Sunset Laboratory, USA)

164   on a separate round filter piece (17 mm diameter) by using the IMPROVE TOT protocol

165   (Bai et al., 2020). In addition, the residual OC and EC contents in samples after

166   methanol extraction were determined with the same method mentioned above, and were

167   subtracted from the total OC content, to derive the methanol-soluble OC (MSOC) (μg

168   C m^{-3}).

169   **2.2.2 Bulk analysis of organics**

170   We employed specially an Aerodyne soot particle AMS (SP-AMS) to determine

171   the bulk composition of water-soluble OA (WSOA) (Onasch et al., 2012). The analysis

172   procedure is similar to that described in Ge et al. (2017). In brief, eight round pieces

173   (20 mm diameter) of each filter were sonicated in 40 mL of ultrapure water, and the

174   aqueous extract was nebulized using an atomizer (TSI, Model 3076), then the mist was

175   dried by a silica gel diffusion dryer and the remaining particles were sent to the SP-

176   AMS. The SP-AMS was operated in a laser-off mode, therefore to measure non-

177   refractory species that can be rapidly vaporized at 600 °C (SP-AMS oven temperature).

178   Note the SP-AMS employs a 70 eV electron impact (EI) ionization scheme, therefore

179   the vaporized species are fragmented into positively charged ions with specific mass-

180   to-charge (m/z) ratios and we obtained the composition of WSOA in the form of lumped

181   molecular fragments rather than detailed molecular composition.

182   The SP-AMS data were post-processed using the Igor-based ToF-AMS analysis

183   toolkit (SQUIRREL version 1.56D and PIKA version 1.15D), Elemental ratios

184   including hydrogen-to-carbon (H/C), oxygen-to-carbon (O/C) and nitrogen-to-carbon

185   (N/C) as well as the organic mass to organic carbon (OM/OC) ratio were calculated by

186   using the methods proposed in Aiken et al. (2008), Canagaratna et al. (2015) and Ge et

187   al. (2024). The WSOA mass concentration of each sample was normalized by

188 multiplying the WSOC concentration with its corresponding OM/OC. Then, we

189 conducted the PMF analysis to resolve the sources of WSOA by utilizing the PMF

190 evaluation toolkit (Version 2.06) (Ulbrich et al., 2009), followed strictly the protocol

191 described in Zhang et al. (2011). As usual, we included only ions with $m/z \leq 120$, and

192 PMF solutions were explored by varying the number of factors (from 3 to 8) and the

193 rotation parameter (f_{peak}, from -1 to 1 with an increment of 0.2). Based on the diagnostic

194 plots in Fig. S1 in the supplement, the four-factor solution was selected as the best

195 solution. The four factors include a hydrocarbon-like OA (HOA) relevant with fossil

196 fuel combustion, a biomass burning-related OA (BBOA), a less oxidized oxygenated

197 OA (OOA1) and a more oxidized oxygenated OA (OOA2) (see details in Sect. 3.1.2).

198 **2.2.3 Molecular characterization of organics**

199 Molecular-level characterization of organic species was conducted by using an

200 ultra-high performance liquid chromatography with a quadrupole time-of-flight (QTOF)

201 mass spectrometer (UPLC-QTOF-MS) (ACQUITY UPLC H-Class coupled with a

202 Xevo G2-XS QTOF, Waters). The sample pretreatment was described in Text S1.

203 Compound separation was performed with a Luna Omega 1.6 μm C18 column (100

204 mm × 2.1 mm × 1.6 μm), and the sample aliquot was subjected to electrospray

205 ionization (ESI), and detected in both positive and negative ion modes. The scanning

206 m/z range for each mass spectrum was 50-1200, with a scanning rate of one spectrum

207 per 0.1 second. More details are presented in Text S2.

208 The original UPLC-QTOF-MS data were processed using the Mass Spectrometry-

209 Data Independent Analysis (MS-DIAL, version 4.92) software (Tsugawa et al., 2015),

210 including peak extraction, alignment and deconvolution, achieving a detection

211 probability of 70% in all samples for any identified compound. The method of

212 systematic error removal using random forest (SERRF, a ML algorithm), was then

213 introduced to reduce systematic errors and normalize the measured data (Fig. S2). All

214 deconvoluted spectra were imported into the SIRIUS (Version 5.6.2) toolkit (Dührkop

215 et al., 2019) to determine molecular formulas. The semi-quantitative concentrations of

216 identified molecules were expressed in the normalized peak areas (NPRs), defined as

217   their peak areas acquired from SERRF divided by air volumes of the samples.

218   In addition, the double-bond equivalent (DBE) was used to indicate the level of

219   unsaturation of the compound (Bae et al., 2011), and the aromaticity equivalent (Xc)

220   (Yassine et al., 2014) was used to indicate the molecular structure. O/C, H/C and DBE

221   values of the sample were averaged over all identified molecules based on their relative

222   abundances (See details in Text S3).

223

224   **2.3 Optical analyses**

225   **2.3.1 Light absorption properties**

226   The light absorption spectra of WSOC and MSOC in 200 ~ 800 nm were obtained

227   using a UV-Vis spectrophotometer (UV-3600, Shimadzu, Japan) with a 0.5 nm interval.

228   The absorbance at a certain wavelength λ (A_λ) were corrected by subtracting that at 700

229   nm (A_{700}) (near zero, as background), and the corresponding light absorption coefficient

230   (Abs_λ, M m^{-1}) is calculated as below (Hecobian et al., 2010):

$$Abs_\lambda = (A_\lambda - A_{700}) \times \frac{V_l}{V_a \times L} \times \ln(10) \qquad (1)$$

232   Where V_l represents volume of the extract (water or methanol), V_a denotes air

233   volume of the filter piece, and L is the optical path length (0.01 meters here).

234   The corresponding mass absorption efficiency (MAE_λ, m^2 g^{-1}) can then be

235   calculated below:

$$MAE_\lambda = \frac{Abs_\lambda}{[WSOC] \ ([MSOC])} \qquad (2)$$

237   Where [WSOC] ([MSOC]) represents the mass concentration of WSOC (MSOC).

238   Following previous studies (Laskin et al., 2015; Chen et al., 2018; Xie et al., 2020;

239   Chen et al., 2020b), the light absorption at 365 nm (Abs_{365}) was employed as a surrogate

240   for BrC in this work.

241   The relationship between the Absorption Ångström Exponent (AAE)(an index of

242   the wavelength dependence) (Andreae and Gelencsér, 2006) and light absorption is

243   shown below:

$$Abs_\lambda = K \cdot \lambda^{-AAE} \qquad (3)$$

245   Where K is a constant related to light absorption, and we computed the AAE values

246   in the 300 ~ 450 nm range.

247   The direct radiative forcing effect of BrC can be represented by the simple forcing

248   efficiency (SFE) (in W g^{-1}), which is the energy added to the earth-atmosphere system

249   per unit mass of aerosol (Bond and Bergstrom, 2006). The SFE of BrC at the

250   wavelength λ can be expressed below (Chen and Bond, 2010):

251

$$\frac{dSFE}{d\lambda} = -\frac{1}{4}\frac{dS(\lambda)}{d\lambda}\tau_{atm}^2(\lambda)(1 - F_C)$$
$$[2 \times (1 - \alpha_S)^2\beta(\lambda)MSE(\lambda) - 4 \times \alpha_S \times MAE(\lambda)]d\lambda \qquad (4)$$

252   Where S(λ) represents the solar irradiance at λ obtained from the ASTM G173–03

253   reference spectra. τ_{atm} denotes the atmospheric transmission (0.79), F_C is set to 0.6,

254   indicating the fraction of cloud cover, the global average value of α_s is fixed at 0.19,

255   representing the surface albedo, β is the backscatter fraction, and MSE and MAE are

256   the mass scattering efficiency and mass absorption efficiency of BrC, respectively. .

257   When estimating the radiative effect of BrC, the direct radiative forcing caused by

258   aerosol scattering can be neglected. Therefore, the absorbed radiative forcing within a

259   given spectral range is calculated by the simplified Eq. (5):

260

$$SFE = \int \frac{dS(\lambda)}{d_\lambda}\tau_{atm}^2(\lambda)(1 - F_C) \times \alpha_S \times MAE(\lambda)\, d\lambda \qquad (5)$$

261   **2.3.2 Fluorescence properties**

262   Characterization of excitation-emission matrix (EEM) of the extracts was

263   performed using a fluorescence spectrophotometer (Cary Eclipse, Agilent, USA) The

264   wavelength range of excitation was set from 230 to 500 nm, and that of emission was

265   from 250 to 600 nm, the scanning resolutions of excitation and emission were 5 nm and

266   2 nm, respectively, with the scanning speed of 1200 nm min^{-1}. The photomultiplier tube

267   (PMT) detector voltage was set at 600 V. The measurement was subjected to instrument

268   calibration, internal filter correction, Raman/Rayleigh scattering correction, and all

269   EEM spectra were subjected to blank filter subtraction. The processed data were further

270   analyzed using the parallel factor analysis (PARAFAC) to group potential components

271   with similar fluorescent properties. The analysis was performed using MATLAB 2022b

272   software with the drEEM toolbox (Murphy et al., 2013).

273   Fluorescent properties of the extracts were also characterized by the humification

274   index (HIX), biological index (BIX), and fluorescence index (FI). HIX is defined as the

275   ratio of integrated fluorescence emission intensity in the range of 435 - 480 nm to that

276   in the range of 300 to 345 nm when excited at 254 nm; BIX is calculated as the ratio of

277   emission intensity at 380 nm to that of 430 nm for the excitation wavelength of 310 nm;

278   FI is the ratio of emission intensity at 470 nm to that of 520 nm under a fixed 370 nm

279   excitation wavelength (Birdwell and Engel, 2010; Mcknight et al., 2001).

280

281   **2.4 Machine learning screening of key light-absorbing species**

282   The ML RF model was used here to screen the key light absorbing species by

283   linking the target variable (Abs_{365}) with the identified organic molecules (in NPRs), via

284   the "randomforest()" function in R software (Version 4.3.2). The model included 500

285   decision trees and estimated the variance through a cross-validation during training.

286   The dataset was divided into a training set (80% of total) and a test set (20% of total)

287   to assure accuracy and robustness of the model.

288   The model outputted two key indices to assess the importance of each molecule to

289   the light absorption. One metric is IncNPu_val, which can measure the purity of nodes.

290   During the construction of each tree in the RF model, each split can increase the purity

291   of nodes, therefore if more frequently a variable is used in splitting, more contribution

292   it has to the increase of purity of nodes, then the variable is considered to be important.

293   IncMSE_val is another index based on the mean squared error (MSE). When we

294   permute a variable, increase in the projected error can serve as a measure of its

295   importance. If a variable with a significant impact on the predicted results is permuted,

296   the model's MSE would increase significantly, resulting in a high IncMSE_val value

297   (González et al., 2015). Under the 50th percentile of IncMSE_val, some variables had

298   zero or even negative contributions to IncMSE_val. Considering the definition of

299   IncMSE_val, such variables would have either no or negative influence on model fitting,

300   thus only the top 50 % of compounds were chosen. Afterwards, intersection of the two

301   indices were considered as potential BrC chromophores.

302   Moreover, a molecule typically requires a substantial uninterrupted conjugation on

303   its molecular backbone to effectively absorb visible light (Lin et al., 2018), therefore a

304   compound with the ratio of DBE to carbon (DBE/C) greater than that of linear polyenes

305   (with a molecular formula of C_xH_{x+2}, DBE/C = 0.5) (Cain et al., 2014) is treated as a

306   potential BrC compound. Besides, the DBE/C ratio should be less than the upper limit

307   of DBE for natural compounds (DBE/C = 0.9) (Lobodin et al., 2012). Finally, the

308   candidate compounds passed aforementioned procedures were compared with those in

309   open-source databases, including MoNA (https://mona.fiehnlab.ucdavis.edu/) and

310   MassBankEU (https://massbank.eu/), to be interpreted as the key BrC compounds.

311

312   **3 Results and discussion**

313   **3.1 Chemical properties**

314   **3.1.1 General characteristics**

315   During the sampling period, the temperatures were 34.34 ± 3.23 °C (daytime) (±

316   one standard deviation, hereinafter) and 30.85 ± 2.97 °C (nighttime) during SS, 13.00

317   ± 6.04 °C (daytime) and 9.97 ± 5.04 °C (nighttime) during CS, and the relative humidity

318   (RH) levels were 53.61 ± 10.33 % (daytime) and 65.88 ± 9.87 % (nighttime) during SS,

319   47.81 ± 18.94 % (daytime) and 55.56 ± 15.74 % (nighttime) during CS, respectively

320   (Figs. 1a and b). Figure 1c depicts the temporal variations of different components.

321   Average concentrations of OC, EC, WSOC, MSOC and total ionic species during

322   daytime and nighttime in the two seasons are summarized in Table 1. Clearly,

323   concentrations of all components were higher in CS than those in SS, but the

324   daytime/nighttime differences were relatively small in both seasons. Also, the MSOC

325   levels were larger than WSOC in all samples. MSOC occupied 82.4 % and 81.5 % while

326   WSOC occupied 61.3 % and 49.5 % of the total OC during SS and CS, respectively,

327   indicating that methanol can more effectively extract the aerosol organics than water.

328   The mean mass contributions of different ions to their total during SS and CS,

329   respectively are shown in Fig. 1c too. The particles were overall neutral as the molar

330   ratios of inorganic anions to cations were 0.97 and 0.98 during SS and CS, respectively

331   (Fig. S3). The most abundant ion was sulfate in SS (45.5 %) and nitrate in CS (50.7 %),

332   as low temperatures during CS favor the partitioning of nitrate to particle phase. As so,

333 the sulfur oxidation ratio (SOR, $[SO_4^{2-}]/([SO_4^{2-}]+[SO_2])$) and nitrogen oxidation ratio

334 (NOR, $[NO_3^-]/([NO_3^-]+[NO_2])$) were 0.58 and 0.16 (daytime) and 0.56, 0.17 (nighttime)

335 during SS, 0.40, 0.28 (daytime) and 0.42, 0.30 (nighttime) during CS, respectively.

336 NOR was indeed much higher in CS especially during nighttime than those in SS.

337 Furthermore, ammonium (NH_4^+) was the predominant cation while sulfate, nitrate and

338 chloride were major anions. The scatter plots of molar concentrations of ammonium

339 versus summed sulfate, nitrate and chloride (Fig. S4) reveal different bonding forms of

340 the aerosol inorganic salts in different seasons. The correlations were both tight

341 (correlation coefficients close to 1) yet the fitted slopes during SS were 0.80 (daytime)

342 and 0.89 (nighttime) while those during CS were 0.98 (daytime) and 0.99 (nighttime),

343 respectively. Such results demonstrate that ammonium was deficit to neutralize the

344 cations therefore significant amounts of metal salts (such as sodium/calcium

345 sulfate/nitrate) could exist during SS while during CS, most inorganic species were in

346 the forms of $(NH_4)_2SO_4$, NH_4NO_3 and NH_4Cl with no appreciable metal salts.

347 **3.1.2 Features and sources of water-soluble organics**

348 Regarding the water-soluble portion of organic species (WSOA), Figure 2a

349 presents the average high resolution mass spectra (HRMS) during SS and CS,

350 respectively. It can be seen that, WSOA during CS appeared to be much more

351 oxygenated than that during SS (O/C: 0.58, 0.59 vs. 0.44, 0.45) . To further unravel

352 causes of such differences, PMF analysis were conducted and the HRMS of resolved

353 factors are presented in Fig. 2b, while mass contributions of these factors during SS and

354 CS as well as the Pearson's correlation coefficents (r) of these factors with other

355 components are illustrated in Fig. 3.

356 The HOA MS was dominated by $C_xH_y^+$ ions (57.2 %), such as $C_4H_7^+$ (*m/z* 55) and

357 $C_4H_9^+$ (*m/z* 57), primarily originating from hydrocarbons emitted from fossil fuel

358 combustion (such as traffic) (Canagaratna et al., 2004). Among the four factors, HOA

359 exhibited the lowest O/C ratio (0.24) and the highest H/C ratio (1.66). The second factor

360 was identified as BBOA, since it has distinct peaks at *m/z* 60 (mainly $C_2H_4O_2^+$, 0.76 %

361 of the total MS) and *m/z* 73 (mainly $C_3H_5O_2^+$, 1.09 % of the total MS), which are

362   characteristic fragments associated with levoglucosan, a tracer compound of biomass

363   burning particles (Kumar et al., 2022; Qin et al., 2017). Correlations between BBOA

364   and these two tracer ions were indeed tight (0.71 with $C_2H_4O_2^+$ and 0.82 with $C_3H_5O_2^+$).

365   A notably positive correlation between BBOA and K^+ (Fig. 3b) further supports its BB

366   origin as K^+ is also a common BB emission tracer (Yu et al., 2018). Note the BBOA

367   here had a relatively higher O/C ratio of 0.61 than those identified in previous offline

368   AMS measurements, such as Yangzhou (0.45) (Ge et al., 2017), Beijing, China (0.59)

369   (Qiu et al., 2019), and Marseille, France (0.54) (Bozzetti et al., 2017), suggesting the

370   potential presence of partially aged BBOA components in this factor.

371   The other two factors are secondary. OOA1 was less oxidized with a O/C of 0.39

372   and OOA2 was more oxygenated with the highest O/C of 0.65 among all factors. OOA1

373   had characteristic fragments at m/z 29 (CHO^+) and m/z 43 (mainly $C_2H_3O^+$) while

374   OOA2 had the least fraction of oxygen-free $C_xH_y^+$ ions (28.5 %) but the largest fraction

375   of oxygenated ions (32.8 % of $C_xH_yO_1^+$ and 18.9 % of $C_xH_yO_2^+$) among the four factors.

376   OOA2 also correlated well with CO_2^+ (m/z 44) ion (r of 0.81), a characterisitic ion of

377   highly oxygenated carboxylic/dicarboxylic acids. Moreover, OOA2 had the highest

378   N/C of 0.095 as well as those of $C_xH_yN^+$ (9.1 %) (such as CH_2N^+, CHN^+ and CH_4N^+)

379   and $C_xH_yO_zN^+$ (3.8 %) (such as $CHON^+$, CH_2NO^+ and CH_4NO^+) ions, indicating the

380   presence of amines and amino acids correspondingly (Ge et al., 2024). Besides, the N/C

381   level of OOA2 is close to that of fogwater observed in Fresno, indicating the aqueous

382   phase reactions are likely an source of those nitrogen-containing ions in OOA2 (Kim et

383   al., 2019). In addition, sulfur-containing organic ions (such as CH_2S^+, $CH_3SO_2^+$ and

384   CHS^+) were almost exclusively present in OOA2 and in a significant fraction (2.7 %),

385   as such ions were strongly associated with aqueous/heterogenous reactions (Zorn et al.,

386   2008; Huang et al., 2020; Petters et al., 2021; Mcneill, 2015), reassuring that OOA2

387   was probably linked with aqueous/heterogenous formation pathway.

388   The time series of mass contributions of the four PMF factors are shown in Fig.

389   1d, and significant differences can be observed during the two sampling seasons, as can

390   be seen clearly in Fig. 3a. HOA was a significant source in both SS and CS, and as

391 expected, it was higher during daytime due to the stronger traffic activities. BBOA was

392 much less important than HOA, but its contribution during CS was obviously more than

393 that during SS (12.5 ~ 13.0 % vs. 7.2 ~ 7.8 %), and accordingly, HOA contribution was

394 slightly larger during SS than during CS (38.0 ~ 41.7 % vs. 29.9 ~ 36.8 %). The most

395 striking difference lies in two SOA factors. OOA1 occupied nearly half of the total

396 WSOA (47.5 ~ 49.8 %) while contributions of OOA2 were only 3.0 ~ 5.0 % during SS;

397 on the other hand, OOA2 occupied 38.6 ~ 43.5 % of WSOA mass while those of OOA1

398 were down to 11.6 ~ 14.1 %. The much larger OOA2 fraction during CS explains its

399 overall high oxidation degree depicted in Fig. 2. These results are well consistent with

400 our previous studies, as we show that during summer in Nanjing, photochemical

401 reactions dominate the SOA formation and yield relatively less oxygenated OA (Xian

402 et al., 2023; Wang et al., 2022b), while during cold seasons, aqueous formation of SOA

403 becomes more important which can generate highly oxygenated OA (Wu et al., 2021).

404 The air temperature (a solar radiation indicator) and ozone (a photochemical product)

405 both correlated positively with OOA1 but negatively with OOA2 (Fig. 3b), further

406 verifying the dominance of photochemical pathway of OOA1 not OOA2. As is well

407 known, particulate nitrate was strongly associated with heterogenous reactions and gas-

408 to-particle partitioning favored by low temperature and high RH especailly during CS,

409 and indeed, OOA2 correlated much tighter with NH_4NO_3 than OOA1 did.

410

411 **3.2 Optical properties**

412 **3.2.1 Light-absorbing properties of WSOC and MSOC**

413 The average light absorption coefficients of BrC in WSOC and MSOC in 300 ~

414 700 nm during daytime and nighttime of SS and CS are illustrated in Fig. 4a. As

415 expected, the values all exponentially decreased as a function of wavelength. The

416 calculated AAE values are listed in Table 1. It is interesting to find that the WSOC AAE

417 had no significant difference between SS and CS (6.35 vs. 6.43), while that of MSOC

418 AAE appeared to be notable (5.99 vs. 6.89); Compared with the MSOC AAE, the

419 WSOC AAE was higher during SS but smaller during CS. The AAE values obtained

420   here are slightly smaller than those reported in Beijing (7.3 ~ 7.5 of WSOC) (Du et al.,

421   2014; Chen et al., 2016), comparable to that in Guangzhou (6.7 of WSOC) (Fan et al.,

422   2016). Note Chen and Bond (2010) reports that particles generated from smoldering of

423   various types of wood exhibit a AAE of 6.9 ~ 11.6 (MSOC); Lambe et al.(2013) shows

424   that lab-generated secondary BrC possesses a AAE of 5.2 ~ 8.8 (MSOC). Compared

425   with these values, our measured AAE values (<7) here probably suggest a dominance

426   of secondarily formed BrC for both WSOC and MSOC. This can be verified by Fig. 3a

427   for WSOC, as indeed it was dominated by SOA particularly during nighttime in both

428   seasons. However, the large difference in WSOA chemical composition in different

429   seasons (especially SOA proportions) did not result in a large difference in WSOC AAE,

430   demonstrating clearly the non-correspondence of chemical species to light-absorbing

431   species (a.k.a., BrC). On the contrary, for MSOC, the relatively large difference of

432   MSOC AAE in different seasons likely reflect the distinction of BrC species but not

433   necessarily chemical constitution. The light absorption coefficients at 365 nm (Abs_{365})

434   are listed in Table 1 too. The average $Abs_{365, WSOC}$ during CS (4.87 M m^{-1}) was

435   approximately 2.15 times that of SS (2.27 M m^{-1}), and that of MSOC during CS (4.97

436   M m^{-1}) was also much larger than that during SS (3.64 M m^{-1}); Nighttime values were

437   higher than those in daytime expect for WSOC during CS. For the same set of samples,

438    $Abs_{365, MSOC}$ values were typically larger than $Abs_{365, WSOC}$ except that CS daytime

439    $Abs_{365, MSOC}$ was slightly smaller than $Abs_{365, WSOC}$ (4.65 vs. 4.89 M m^{-1}). Scatter plots

440   of Abs_{365} versus WSOC (and MSOC), and $Abs_{365, WSOC}$ versus $Abs_{365, MSOC}$ for the four

441   series of samples are given in Fig. S5. The correlations were generally well especially

442   those of WSOC and MSOC ($r > 0.80$), suggesting that there is a large overlap of

443   extracted species between WSOC and MSOC, as well as their BrC constituents.

444   Regarding the MAE at 365 nm (MAE_{365}), $MAE_{365, WSOC}$ during CS (0.75 m^2 g^{-1})

445   was higher than that during SS (0.55 m^2 g^{-1}), indicating its stronger light absorption

446   ability during CS; however, the $MAE_{365, MSOC}$, unlike $Abs_{365, MSOC}$, was smaller during

447   CS than that during SS (0.50 vs. 0.72 m^2 g^{-1}). Besides, MAE_{365} values for both WSOC

448   and MSOC were slightly larger during nighttime than those during daytime in both

449 seasons. Compared to previous winter studies, the $MAE_{365, WSOC}$ in Nanjing here was

450 lower than that in Beijing (1.21 ~ 1.26 $m^2 g^{-1}$) (Du et al., 2014; Chen et al., 2016; Li et

451 al., 2020), similar to our earlier observation in Yangzhou (0.75 $m^2 g^{-1}$), but the $MAE_{365,}$

452 $_{MSOC}$ appears to be less than that in Yangzhou (1.12 $m^2 g^{-1}$)(Chen et al., 2020). To further

453 explain the low MAE_{365} observed here, we investigated the air mass origins of our

454 samples collected in different periods via back trajectory analysis (at an altitude of 200

455 m and 24 hours backwards) using the MeteInfo (Version: 3.0.0) (Wang, 2019). As

456 shown in Fig. S6, only a limited fraction of air mass trajectories passed through sea and

457 coastal areas (clusters 4 and 5, 27.05 % during daytime and 29.54 % during nighttime)

458 during SS, while during CS, proportions of trajectories that intercepted sea/costal air

459 increased to 79.80 % (clusters 1, 2 and 3 during daytime) and 69.44% (clusters 2, 3 and

460 4 during nighttime), respectively. Note the air masses during CS are somewhat unusual

461 as typically they mainly originate from inland regions (Wu et al., 2019b), which might

462 cause the low MAE_{365} observed in this work as particles affected by marine air can be

463 less light-absorptive than those influenced by inland air (Li et al., 2022).

464   Saleh (2020) proposes a method that uses the MAE_{405} (MAE at 405 nm) – AAE

465 two-dimension space to assess the light-absorbing ability of BrC, as shown in Fig. 4b.

466 The majority of samples in this study fall into the regime of W-BrC (weakly light-

467 absorptive BrC) with a few MSOC samples locating in the VW-BrC (very weak BrC)

468 regime, which are similar to a few other observations (Zhou et al., 2021; Xu et al., 2022).

469 The BrC in MSOC seemed to cover a broader region than it in WSOC, indicating that

470 the MSOC BrC might contain a wider array of species and/or originate from more

471 diverse sources/processes. Daytime/nighttime difference of MSOC BrC was also more

472 obvious than that of WSOC BrC.

473   At last, we estimated the SFE values of WSOC and MSOC in the range of 300–

474 700 nm, considering the actual visible light wavelength as well as the negligible light

475 absorption above 700 nm of BrC. As summarized in Table 1, the mean SFE_{MSOC} (2.43

476 W g^{-1}) during SS was higher than that of WSOC (2.20 W g^{-1}), but it became smaller

477 during CS (2.23 W g^{-1}) and was much lower than that of WSOC (3.24 W g^{-1}). The

17

478   SFE$_{WSOC}$ values in both SS and CS were lower than that in Beijing (4.6 ± 1.7 W g^{-1} in

479   summer and 6.2 ± 2.0 W g^{-1} in winter), especially in CS (Deng et al., 2022). For both

480   WSOC and MSOC, SFE values during nighttime were slightly larger.

3.2.2 Source apportionment of light absorption of WSOC

482   In Sect. 3.1.2, sources of WSOA were identified and quantified, herein we applied

483   a multiple linear regression (MLR) algorithm to apportion the light absorption of

484   WSOC to these sources. The scatter plot of reconstructed Abs$_{365, WSOC}$ versus measured

485   values are shown in Fig. S7. The fitted slope is 1.06 with a Pearson's r of 0.90, verifying

486   the robustness of this method on our dataset. The calculated regression coefficients,

487   representing the factors' MAE$_{365}$ values (m² g^{-1}) are listed in Table 2. Compared to our

488   earlier results in Yangzhou (Chen et al., 2020b), the HOA MAE$_{365}$ (0.71 m² g^{-1}), was

489   much less than that in Yangzhou (1.46 m² g^{-1}), while the BBOA MAE$_{365}$ values were

490   similar (0.71 vs. 0.77); MAE$_{365}$ values of OOA1 (0.12 m² g^{-1}) and OOA2 (0.83 m² g^{-1})

491   were very close to the two SOA factors in Yangzhou (0.11 and 0.85 m² g^{-1}). However,

492   here the less oxygented OOA1 has the small MAE$_{365}$ while in Yangzhou, the more

493   oxygenated SOA has the similar MAE$_{365}$ as OOA1, and *vice versa* for the other pair.

494   This work finds that the more oxidized SOA has a stronger light absorption ability,

495   opposite to that reported in Yangzhou. Nevertheless, the two findings are not

496   contradictory with each other, as atmospheric ageing can lead to either photo-

497   enhancement or photo-bleachment, dependent upon the precursors. For instances,

498   aqueous oxidation of BBOA can increase (Gilardoni et al., 2016) yet conversely

499   aqueous processing of fossil fuel combustion OA can decrease the light absorptivity of

500   OA (Wang et al., 2021). As discussed in Sect. 3.2.1, the unusual air masses during CS

501   in this work clearly indicate different precursors from those in Yangzhou.

502   The average contributions of HOA, BBOA, OOA1 and OOA2 to Abs$_{365, WSOC}$

503   across the whole campaign were 33.05 %, 15.49 %, 6.00 % and 45.46 %, respectively

504   (Table 2). Figure 5 further presents contributions of the factors under different scenarios.

505   Compared with their mass contributions shown in Fig. 3a, during SS, the dominant

506   contributor of light absorption became HOA (daytime 63.7 %, nighttime 55.6 %), and

507   contributions of BBOA and OOA2 both increased relative to their mass fractions; while

508   OOA1's contribution was largely reduced to 15.0 ~ 16.2 % due to its small MAE_{365}.

509   Previous studies have consistently identified coal combustion (Fan et al., 2016; Li et al.,

510   2019; Song et al., 2019) and traffic emissions (Hecobian et al., 2010) as significant

511   contributors to BrC, together with our results here, highlighting the substantial impact

512   of anthropogenic fossil fuel combustion on atmospheric visibility. During CS, OOA2

513   dominated the light absorption (daytime 50.7 %, nighttme 63.0 %) owing to its large

514   mass contribution as well as large MAE_{365}; OOA1 became a very minor contributor

515   (2.1 ~ 2.8 %), HOA contribution decreased while BBOA contribution increased relative

516   to their mass fractions. Overall, we find that primary fossil fuel combustion emissions

517   govern water-soluble BrC light absorption during SS especailly during daytime, while

518   during CS, secondary highly aged species (likely from aqueous/heterogenous reactions)

519   dominates, especially during nighttime.

520   To further explore the impact of atmospheric ageing on BrC, we plotted MAE_{365}

521   as a function of O/C in Fig. 6. Interestingly, during SS, MAE_{365} generally decreased

522   with the increase of O/C, especially in daytime as its fitted slope of -1.56 was over 2

523   times that of nighttime (-0.76). On the other hand, MAE_{365} showed an increasing trend

524   against O/C during CS, particularly in nighttime as the fitted slope was 1.43, larger than

525   that of daytime (1.12). These results further supports our earlier findings and underscore

526   that during summer photochemical reactions can lead to photo-bleachment of aerosols

527   while during cold seasons aqueous/heterogenous reactions might dominate the

528   secondary formation and lead to photo-enhancement; clearly, photochemical oxidation

529   and aqueous/heterogenous reactions are more active during daytime and nighttime,

530   respectively, consistent with the slopes in Fig. 6. Also, photochemcially produced SOA

531   was often less or moderately oxygenated and that from aqueous/heteregenous oxidation

532   was more oxidized, and there is a turning point at O/C of 0.45 ~ 0.5 in the MAE_{365}-O/C

533   plot, which was found in previous studies too (Zhong et al., 2023; Jiang et al., 2022).

534   **3.2.3 Fluorescent properties of WSOC and MSOC**

535   The fluorescence indices like HIX, BIX and FI, can infer the types and sources of

536   dissolved organic matter (DOM) in aquatic systems and soils (Lee et al., 2013; Huguet

537   et al., 2009). Recently, these indices have been employed to investigate sources and

538   aging processes of atmospheric OA (Fu et al., 2015; Qin et al., 2018; Deng et al., 2022;

539   Murphy et al., 2013). Here, we calculated these indices for both WSOC and MSOC.

540   HIX represents the degree of humification, and a high HIX means high

541   aggregation, C/H ratio and aromaticity of the organics (Zsolnay et al., 1999; Mcknight

542   et al., 2001; Birdwell and Engel, 2010), thus it normally increases upon ageing (Fan et

543   al., 2019; Murphy et al., 2013). In this study, HIX of WSOC during SS and CS were on

544   average 3.34 and 4.68, respectively (Table 3), much less than the HIX levels in aquatic

545   or soil DOM (Dong et al., 2017), suggesting an overall low aromaticity of atmospheric

546   OA in Nanjing. As a comparison, the WSOC HIX are higher than those in Colorado,

547   USA (2.42) (Xie et al., 2016) and Tianjin, China (2.73 and 2.22) (Deng et al., 2022),

548   but significantly lower than that in Nanjing during 2017-2018 (7.07) (Xie et al., 2020).

549   An earlier study proposes the HIX ranges of 1.4-5 for fresh SOA and 4.2-6.1 for aged

550   SOA (Lee et al., 2013). Despite influences of other primary sources, the average HIX

551   during SS did fall in the fresh SOA range and the value during CS entered the edge of

552   aged SOA, in line with the oxidation degrees of OA (Fig. 2a) and mass proportions of

553   fresh/aged SOA factors (namely, OOA1/OOA2) (Fig. 3a) during different seasons. The

554   average HIX of MSOC (2.72 and 3.48) were lower than those of WSOC in both seasons,

555   indicating that HULIS with high aromaticity are preferentially soluble in water.

556   FI is indicative of the relative contributions of terrestrial and biogenic sources

557   while BIX, in contrast to HIX, can be treated as a freshness index. A fluorophore is

558   often associated with high aromaticity if FI is low (Fu et al., 2015), and a high BIX

559   indicates a high content of freshly released organics (such as biological or microbial

560   derived species) (Wen et al., 2021; Huguet et al., 2009; Murphy et al., 2013). The

561   average WSOC BIX values during SS and CS were determined to be 0.84 and 0.88,

562   respectively, with corresponding FI of 1.91 and 1.90 (Table 3), and the corresponding

563   MSOC BIX were 0.90 and 0.96, and MSOC FI were 2.27 and 2.11, respectively.

564   Compared with results during 2017-2018 in Nanjing, BIX and FI values of WSOC were

565   similar, yet those of MSOC here were larger (Xie et al., 2020). Figure 7 shows the

566   measured data in the HIX-FI and HIX-BIX diagrams along with results from a few

567   other studies. It can be seen that, almost all BIX values distributed in the range of 0.6 ~

568   1 (Huguet et al., 2009) and FI values distributed within 1.6 ~ 1.9 (Mcknight et al., 2001),

569   suggesting that OA in both seasons was influenced by a mix of terrestrial and

570   microbial/biogenic sources. For both WSOC and MSOC, BIX was slightly higher

571   during CS than during SS, attributing to the fact that OA during CS contained more

572   aged SOA species. Nearly no difference for WSOC FI during different seasons were

573   observed, but the MSOC FI during CS was slightly lower than that during SS, meaning

574   that MSOC during CS had a high aromaticity as expected. In addition, BIX and FI

575   values during nighttime were marginally higher than those during daytime in all cases.

576   **3.2.4 Identification of key fluorophores of WSOC and MSOC**

577   The 3D EEM-PARAFAC analysis was adopted to identify the key fluorophores of

578   BrC, with results in Fig. 8 and Fig. S8. Four components were resolved for both WSOC

579   and MSOC. For WSOC, C1 exhibited a peak at Ex = 230 nm and Em = 374 nm,

580   identified as less oxidized HULIS typically associated with combustion sources. Its

581   contribution was only 4.9 % during SS but increased to 19.2 % during CS (Fig. S8a).

582   C2 had a prominent peak at Ex = 230 nm and Em = 396 nm and a second peak at Ex =

583   320 nm and Em = 396 nm, classified as a HULIS-related component too, as the dual-

584   peak distribution of fluorescence spectrum is often associated with HULIS (Coble,

585   1996; Murphy et al., 2011; Yu et al., 2015); its second peak indicates the abundance of

586   compounds with condensed aromatics, conjugated bonds, and non-linear rings (Matos

587   et al., 2015). C2 contribution was comparable during different seasons (37.5 % vs.

588   38.6 %), and it seemed to be more important in nighttime than in daytime (44.0 % vs.

589   26.9 % during SS, and 41.4 % vs. 34.8 % during CS). C3 component, with a peak at Ex

590   = 240 nm and Em = 446 nm, was considered as a highly oxidized HULIs component,

591   relevant with secondary processes (Cheng et al., 2016; Cao et al., 2021). Hawkins et al.

592   (2016) and Aiona et al. (2017) reported fluorescent pattern of products from aqueous-

593   phase reaction of aldehydes with ammonium sulfate or amines (Ex < 250/300 nm and

594   Em > 400 nm) well matches the pattern identified here. As discussed earlier,

595   aqueous/heterogenous reactions contributed to WSOA, especailly during CS;

596   correspondingly, C3 contribution was indeed much higher during CS than during SS

597   (24.1 % vs. 14.7 %). C4, with a prominent peak at Ex = 230 nm and Em = 308 nm and

598   a second peak at Ex = 275 nm and Em = 305 nm, was characterized as a protein-like

599   component (Yan and Kim, 2017; Wu et al., 2019a; Chen et al., 2020b). C4 was the

600   single largest contributor (42.9 %) during SS particualy during daytime (55.0 %), but

601   became the least one during CS (18.0 %), indicating distinct fluorescent properties of

602   OA in different seasons. Overall, since C1 ~ C3 are all relevant with HULIS, the WSOC

603   fluorescent properties were governed by HULIS (57.1 % in SS and 82.0 % in CS).

604   Similarly for MSOC, three HULIS-related fluorophores (C1 ~ C3) and one

605   proteinaceous fluorophore (C4) were separated (Fig. 8b). The spectral signatures

606   between the two series of fluorophores were slightly different, with the MSOC peak

607   excitation and emission wavelengths being a bit larger than those of WSOC, especially

608   for C2 and C3. Figure S8b shows contributions of the different components to MSOC

609   fluorescene. C1 was much more important in MSOC (26.6 % in SS and 39.2 % in CS)

610   than in WSOC, and became the largest contributor of MSOC during CS; summed C2

611   and C3 contributions (30.7 % in SS and 37.0 % in CS) were on the other hand much

612   less than in WSOC; C4 remained to be the largest (42.6 %) similar to that in WSOC

613   during SS. It is worth to point out that C4 not only contains proteinaceous species like

614   tyrosine and tryptophan but also certain PAHs or phenolic substances emitted from

615   fossil fuel and/or biomass burning, especially in urban aerosols (Barsotti et al., 2016;

616   Chen et al., 2021; Chen et al., 2020b; Cao et al., 2021; Deng et al., 2022). Probably, the

617   proteinaceous species dominated the fluorescence during SS for both WSOC and

618   MSOC, while during CS PAHs and phenolic compounds became more important and

619   they might prefer to dissolve in methanol therefore lead to a higher contribution in

620   MSOC than in WSOC (23.8 % vs. 18.0 %). Daytime/nighttime variations of MSOC

621   were similar to those of WSOC, as shown in Fig. S8.

622

3.3 Molecular composition of organics

3.3.1 Overview of identified molecules

We classified the identified molecular formulas of organics via UPLC-QTOF-MS analysis into 8 categories, namely CH, CHO, CHN, CHS, CHON, CHOS, CHNS, and CHONS. Overall, the negative (ESI$^-$) and positive (ESI$^+$) ion modes identified 466 ~ 865 and 644 ~ 1065 formulas, respectively (details in Table S1). Figures S9 and S10 shows the number and signal fractions (relative abundances of signal intensities) of different classes of compounds, respectively.

Under ESI$^+$ mode, CHON compounds were the most abundant species in term of the number fraction – nearly half during SS (daytime 50.5 % and nighttime 46.9 %), and over half during CS (daytime 54.1 % and nighttime 55.1 %), and the abundance of its signal was even more prevailing – over half in all cases and up to 67.7 % during SS daytime; the second abundant species were CHO compounds, occupying 23.0 ~ 30.6 % of the total number of molecules and 15.4 ~ 21.9 % of the total signal intensity; CHONS and CHN species were the other two relatively abundant classes – together occupying ~ 20 % (number fraction) and ~ 10 ~ 24 % (signal fraction) of total identified compounds; contributions of other four classes of compounds were very minor, in terms of both number and signal intensity. Relatively, under ESI$^-$ mode, CHO compounds marginally prevailed over CHON compounds in number (36.2 ~ 44.4 % vs. 32.6 ~ 38.0 %), but during CS their signal fractions were still lower (33.3 ~ 35.1 % vs. 39.3 ~ 46.5 %). More enrichment of CHO compounds in ESI$^-$ than in ESI$^+$ is consistent with a previous work (Lin et al., 2012) as these compounds most likely contain carboxyl groups and are easily deprotonated in ESI$^-$ mode. Number fractions of CHONS compounds in ESI$^-$ mode were ~5 ~ 10% more than those in ESI$^+$ mode, while the most contrasting difference was that CHN compounds were rarely detected in ESI$^+$ mode, and instead CHOS compounds that were negligible in ESI$^-$ mode could be effectively detected in ESI$^+$ mode (3.9 ~ 4.8 % in number) and their signal fractions were more significant (6.4 ~ 17.4 %).

3.3.2 CHO compounds

For the detected CHO compounds, we plotted them in the van Krevelen (VK) diagrams according to their H/C and O/C ratios in Fig. 9. Most molecules had the O/C ratios < 0.5, but a broad distribution of H/C ratios (0.5 ~ 2.0). Molecules with high H/C ratios ($\geq$ 1.5) and low O/C ratios ($\leq$ 0.5) (Region A) were typically associated with aliphatic compounds, while those with low H/C ratios ($\leq$ 1.0) and low O/C ratios ($\leq$ 0.5) (Region B) are usually assigned to oxygenated aromatics (Kourtchev et al., 2014). We further calculated the Xc values of all CHO compounds to investigate their molecular structures in Fig. 9. Clearly, saturated aliphatic CHO compounds (Xc < 2.5) were most abundant (323 out of 418 in ESI$^+$ mode, and 315 out of 481 in ESI$^-$ mode) and mainly distributed in Region A. Appreciate number of unsaturated compounds particularly those with benzene ring or naphthalene ring structures (2.5 <Xc <2.8), distributed across from H/C of 0.5 to 1.75 but with O/C < 0.5 in ESI$^-$ mode and from H/C of 0.1 to 1.75 but with a few in the side of O/C > 0.5.

The oxygenation state (OS$_c$) (Kroll et al., 2011) (defined as 2*O/C - H/C), is another metric to assess the ageing/oxidation degree of a compound. Figure 10 illustrates the dependence of OS$_c$ on carbon number for all CHO compounds. The molecules had a broad coverage of OS$_c$ (-2 to +2) and carbon number (up to 50). Kroll et al. (2011) grouped the compounds into different origins according to their OS$_c$ and C numbers, including fossil fuel combustion HOA, BBOA, semi-volatile oxygenated OA (SV-OOA, typically less-oxidized) and low-volatility oxygenated OA (LV-OOA, typically more-oxidized), as marked in Fig. 10. Obviously, for both ESI$^-$ and ESI$^+$ modes, a large portion of compounds belonged to HOA and BBOA. In ESI$^+$ mode, a significant portion of molecules located in the BBOA region, while in ESI$^-$ mode, more molecules tended to be found in the HOA region, and even more molecules located within HOA regime during CS than during SS (Figs. S11 and S12), indicating large influences from anthropogenic emissions. Besides, the number of nighttime LV-OOA molecules was more than that of daytime particular during CS, acting as a supporting evidence of aqueous/heterogeneous reactions.

3.3.3 CHON and CHN compounds

680

681   We mapped the detected CHON compounds colored by Xc in the VK diagrams

682   shown in Fig. 11. The compounds were sorted into different series according to the

683   functional groups as well. For ESI$^+$ mode (Fig. 11a), the compounds containing a -NO

684   moiety were dominant and a majority of CHON compounds were saturated with Xc <

685   2.5. Among them, $C_6H_{15}NO(CH_2)_n$ might be N,N-diethylethanolamine homologous

686   compounds, and $C_6H_{15}NO_2(CH_2)_n$ might be diisopropanolamine homologous

687   compounds, as both compounds possess lone pair electrons, prone to positive charge

688   (Ge et al., 2011). Unsaturated CHON compounds with $X_C \geq 2.5$ located in the bottom-

689   left corner, such as $C_5H_5NO(CH_2)_n$, $C_7H_7NO(CH_2)_n$, $C_8H_7NO(CH_2)_n$, and

690    $C_9H_7NO(CH_2)_n$, likely homologous compounds of hydroxypyridine, benzamide,

691   4hydroxy-benzene acetonitrile, and hydroxyquinoline, respectively (Ma and Hays,

692   2008; Wang et al., 2020). In ESI$^-$ mode, the compounds scattered wider than those in

693   ESI$^+$ mode in the VK plot (Fig. 11b), and the majority of them contained one or two

694   nitrogen atoms. Over 25 % of the CHON formulas can be classified as monocyclic or

695   polycyclic compounds with Xc ≥ 2.5 (even up to 68 % during SS daytime; inferred

696   from Figs. S13 and S14). The identified series of homologous compounds mostly

697   situated in the bottom-left corner and also with Xc ≥ 2.5, such as $C_6H_5NO_3(CH_2)_n$,

698    $C_6H_5NO_4(CH_2)_n$, $C_8H_7NO_3(CH_2)_n$, $C_8H_7NO_4(CH_2)_n$, and $C_{10}H_7NO_3(CH_2)_n$, likely

699   nitrophenol, nitrocatechol, nitroacetophenone, nitrophenylacetic acid, and

700   nitronaphthol homologues, respectively (Wang et al., 2018b; Song et al., 2019; Lin et

701   al., 2017; Lin et al., 2015).

702   As stated in Sect. 3.3.1, CHN compounds were only enriched in ESI$^+$ mode. The

703   scatter plot of H/C versus N/C of these compounds is depicted in Fig. 12 (results of

704   different periods are shown in Fig. S15). Similarly, they are colored by Xc and sorted

705   into a number of different series. Most of these compounds were amines with one or

706   two N atoms. The series of aliphatic amines and other monocyclic species with $X_C <$

707   2.71 mostly located in upper part of the plot, including $C_6H_{15}N(CH_2)_n$, $C_5H_{11}N(CH_2)_n$

708   and $C_6H_{12}N(CH_2)_n$, $C_4H_6N_2(CH_2)_n$, $C_5H_6N_2(CH_2)_n$, $C_7H_6N_2(CH_2)_n$, and $C_{11}H_{17}N(CH_2)_n$.

709   Note the presence of 2 N-heterocyclic species was a sign of presence of BBOA (Wang

710   et al., 2017). The series of $C_{10}H_9N(CH_2)_n$ (1N-PAHs) with $X_C \geq 2.71$ may represent the

711   aminonaphthalene homologues (Ge et al., 2011), likely from initial burning of

712   carbonaceous materials (Mao et al., 2022).

713   **3.3.4 CHOS and CHONS compounds**

714   Among the CHOS formulas (only significant in ESI⁻ mode), ones with O/S ratios

715   ≥ 4 were classified as organosulfates (OSs), which were the most abundant type (Table

716   4). Its number fractions were particularly high during CS (daytime 54.3 %, nighttime

717   68.6 %), reiterating the importance of aqueous SOA formation during CS. For the

718   CHONS compounds, in ESI⁻ mode, 5.3 ~ 12.5 % of the formulas had O/(4S+3N) ratios

719   ≥ 1, allowing them to be assigned to –OSO$_3$H and –ONO$_2$ groups, namely nitrooxy-

720   organosulfates (nitrooxy-OSs) (Wang et al., 2018a); while in ESI⁺ mode, 9.8 ~ 11.8%

721   of total CHONS formulas were apportioned as nitrooxy-OSs (Table 4).

722

723   **3.4 Machine learning assisted identification of key BrC molecules**

724   As stated in Sect. 2.4, the ML RF algorithm was used to identify the key BrC

725   chromophores, and we finally confirmed 31 compounds (18 in ESI⁺ mode and 13 in

726   ESI⁻ mode); details regarding their molecular formulas and proposed structures, etc.,

727   are summarized in Table S2. These species are relevant with 4 out of 8 identified types

728   of compounds (CH, CHO, CHN and CHON) (Fig. 13). Note except 6 out of the 31

729   species (4-methylcoumarin, urocanate, 3-hydroxybenzoic acid, chrysin, 2-

730   hydroxypyridine and 4-hydroxyacetophenone), all other species were in general

731   reported as BrC molecules before (See Table S2).

732   Two PAHs (acenaphthylene and fluoranthene, belonging to CH category) in ESI⁺

733   mode were identified, which is reasonable as PAHs are known important BrC (Aurell

734   et al., 2015; Kuang et al., 2021).

735   Twelve CHO compounds (5 in ESI⁺ mode and 7 in ESI⁻ mode) were identified. In

736   ESI⁺ mode, 9-fluorenone and benzanthrone belonging to oxyheterocyclic PAHs (O-

737   PAHs), are known as important BrC chromophores (Kuang et al., 2023); scopoletin is

738 also known as a light-absorbing compound (Zhang, 2018); phthalic anhydride is an

739 oxygen-containing heterocyclic compound. A previous study reports that methanol (the

740 solvent used here) might react with conjugated carbonyl species (such as phthalic

741 anhydride, maleic anhydride, and maleimide) (Chen et al., 2022), thereby affecting the

742 light absorption of relevant BrC species, further studies are needed to verify phthalic

743 anhydride as a key chromophore. In ESI$^-$ mode, a pair of quinone isomers (1-

744 hydroxyanthraquinone and 2-hydroxyanthraquinone) were resolved, in agreement with

745 Kuang et al. (2023), which identified 1-hydroxyanthraquinone as a BrC chromophore

746 in Beijing; 1-hydroxypyrene is a hydroxylated PAHs , also proven as a BrC before

747 (Huang et al., 2022).

748   The identified seven CHN compounds (exclusively in ESI$^+$ mode) included 4 N-

749 heterocyclics, 2 nitro-PAHs, and 1 quinoline compound. It is well known that biomass

750 burning (BB) release a lot of BrC species. As mentioned earlier, CHN compounds are

751 abundant in BB emissions (such as agricultural waste burning and forest fires (Laskin

752 et al., 2009)); small N-containing heterocyclic compounds with one or two aromatic

753 rings, can be effectively produced from thermal decomposition of plants (Ma and Hays,

754 2008), and high temperature pyrolysis of CHN compounds and N-containing plant

755 materials, can result in N-PAHs (Lin et al., 2016). Therefore, identification of the CHN

756 species here as key BrC chromophores are well justified.

757   The remaining confirmed key BrC molecules included 10 CHON compounds (4

758 in ESI$^+$ mode and 6 in ESI$^-$ mode). For ESI$^-$ mode, 3-hydroxyanthranilic acid is an

759 amino phenolic compound $^-$, and the rest five compounds are all nitrophenols, well

760 known as BrC (Li et al., 2020). Another amino phenolic compound, 2-aminophenol was

761 identified in ESI$^+$ mode. Previously, efficient light absorption at 275 nm of 2-

762 aminophenol has been reported, which can be further enhanced in the presence of Fe^{3+}

763 due to formation of oligomers (Al-Abadleh et al., 2022). For acridone in ESI$^+$ mode,

764 earlier studies have shown that acridine exhibits increased light absorbance in the

765 wavelength range of 260 ~ 320 nm under irradiation in N$_2$, air, or O$_2$; additionally, a

766 deep yellow layer forms on the surface, indicating the production of light-absorbing

767   products, which was identified as acridone (Negron-Encarnacion and Arce, 2007).

768

769   **4 Conclusions**

770   This work performed a comprehensive investigation on the chemical and optical

771   properties of BrC in ambient $PM_{2.5}$ samples. Regarding the chemical properties, it was

772   found that methanol was able to extract more OC than water (~82% vs. 49.5 ~ 61.3%

773   of total OC). The WSOA was composed of two primary factors relevant with fossil fuel

774   combustion (HOA) and biomass burning (BBOA), and two SOA factors (a less oxidized

775   OOA1 and a highly oxygenated OOA2). During CS, OOA2 was abundant (38.6 ~

776   43.5 %) while during SS OOA1 was abundant (47.5 ~ 49.8 %); HOA was also an

777   important contributor in both seasons (29.9 ~ 41.7%) but BBOA contribution was

778   relatively minor (7.2 ~ 13.0 %). Further analyses reveal that OOA1 was mainly

779   associated with photochemical reactions while OOA2 was strongly linked with

780   aqueous/heterogeneous reactions. Regarding the light absorption, our observation

781   shows that $Abs_{365, MSOC}$ was typically larger than $Abs_{365, WSOC}$, but though $MAE_{365, MSOC}$

782   was still larger than $MAE_{365, WSOC}$ during SS, it became smaller than the $MAE_{365, WSOC}$

783   during CS, likely owing to that the air mass trajectories during CS significantly

784   intercepted sea/coastal air. The light absorbing abilities of both WSOC and MSOC were

785   weak, but our observations suggest that aqueous oxidation can lead to significant photo-

786   enhancement, therefore the light absorption of WSOA was dominated by OOA2 (50.7

787   ~ 63.0 %) during CS; while photochemical oxidation could cause a photo-bleaching

788   effect and therefore the contribution of OOA1 to WSOA absorbance was small (15.0 ~

789   16.2 %), and HOA contribution was prevailing during SS (55.6 ~ 63.7 %). PARAFAC

790   analysis on the fluorescent spectra of WSOC and MSOC both resolved four key

791   components with slightly differences, including three HULIS component and one

792   protein-like component. HIX, BIX and FI indices also suggest that both WSOC and

793   MSOC originated from a mix of terrestrial and microbial/biogenic sources.

794   The molecular analysis determined 644 ~ 1065 molecules in ESI^+ mode and 466 ~

795   865 molecules in ESI^- mode. Overall, CHON compounds were the most abundant type

796   especially in ESI$^+$ mode, while CHO compounds slightly exceeded CHON compounds

797   in number but were still lower in signal intensity. CHN compounds was the third

798   important class and only detectable in ESI$^+$ mode. The VK diagrams further

799   demonstrate the different aromaticity equivalent (Xc) values and evolution pathways of

800   the different classes of compounds. In addition, significant presence of organosulfates

801   and nitroxy-organosulfates in CS samples especially during nighttime re-affirm the

802   importance of aqueous-phase oxidation during CS. At last, based on the molecular

803   characterization and light absorption measurement results, we applied the ML RF

804   algorithm to identify the key BrC molecules, and we successfully identified 31 key

805   species, including mainly the PAHs, oxyheterocyclic PAHs (O-PAHs), quinones and N-

806   containing compounds. Overall, our findings presented here expand the scientific

807   understanding regarding the chemical composition (both bulk and molecular level) and

808   optical properties (both light absorption and fluorescence) of BrC, and are valuable to

809   evaluate the impact on air quality and radiation balance of BrC. Besides, our identified

810   list of key BrC molecules can be a useful reference for future studies.

811

812   **Code availability.** The software code to analyze the SP-AMS data is publicly available

813   at: https://cires1.colorado.edu/jimenez-

814   group/ToFAMSResources/ToFSoftware/index.html. The software code to analyze the

815   UPLC-QTOF-MS   data   is   publicly   available   at:

816   https://systemsomicslab.github.io/compms/msdial/main.html. The software code using

817   SERRF   to   normalize   UPLC-QTOF-MS   data   is   available   at:

818   https://slfan.shinyapps.io/ShinySERRF/

819

820   **Data availability.** The data in this study are available from the authors upon request

821   (caxinra@163.com).

822

823   **Supplement.** The supplement related to this article is available online at: XXX

824

825 **Author contributions.** YH, XL and DDH conducted the experiments. YH, XL, RL,

826 BZ, YZ and XG performed the data analysis. YH and XG wrote the paper. All authors

827 reviewed the paper and provide useful suggestions.

828

829 **Competing interests.** The contact author has declared that neither they nor their co-

830 authors have any competing interests.

831

832 **Disclaimer.** Publisher's note: Copernicus Publications remains neutral with regard to

833 jurisdictional claims in published maps and institutional affiliations.

834

841

842

843

844 **References**

845 Aiken, A. C., DeCarlo, P. F., Kroll, J. H., Worsnop, D. R., Huffman, J. A., Docherty,

846 K. h. S., Ulbrich, I. M., Mohr, C., Kimmel, J. l. R., Sueper, D., Sun, Y. l., Zhang, Q.,

847 Trimborn, A., Northway, M., Ziemann, P. J., Canagaratna, M. a. R., Onasch, T. B.,

848 Alfarra, M. R., Prevot, A. S. H., Dommen, J., Duplissy, J., Metzger, A., Baltensperger,

849 U., and Jimenez, J. L.: O/C and OM/OC ratios of primary, secondary, and ambient

850 organic aerosols with high-resolution time-of-flight aerosol mass spectrometry, Environ.

851 Sci. Technol., 42, 4478-4485, https://doi.org/10.1021/es703009q, 2008.

852 Aiona, P. K., Lee, H. J., Leslie, R., Lin, P., Laskin, A., Laskin, J., and Nizkorodov,

853 S. A.: Photochemistry of products of the aqueous reaction of methylglyoxal with

854 ammonium sulfate, ACS Earth Space Chem., 1, 522-532,
855 https://doi.org/10.1021/acsearthspacechem.7b00075, 2017.

856 Al-Abadleh, H. A., Motaghedi, F., Mohammed, W., Rana, M. S., Malek, K. A.,
857 Rastogi, D., Asa-Awuku, A. A., and Guzman, M. I.: Reactivity of aminophenols in
858 forming nitrogen-containing brown carbon from iron-catalyzed reactions, Commun.
859 Chem., 5, 112, https://doi.org/10.1038/s42004-022-00732-1, 2022.

860 Andreae, M. O. and Gelencsér, A.: Black carbon or brown carbon? The nature of
861 light-absorbing carbonaceous aerosols, Atmos. Chem. Phys., 6, 3131-3148,
862 https://doi.org/10.5194/acp-6-3131-2006, 2006.

863 Aurell, J., Gullett, B. K., and Tabor, D.: Emissions from southeastern U.S.
864 Grasslands and pine savannas: Comparison of aerial and ground field measurements
865 with laboratory burns, Atmos. Environ., 111, 170-178,
866 https://doi.org/10.1016/j.atmosenv.2015.03.001, 2015.

867 Bae, E., Yeo, I. J., Jeong, B., Shin, Y., Shin, K. H., and Kim, S.: Study of double
868 bond equivalents and the numbers of carbon and oxygen atom distribution of dissolved
869 organic matter with negative-mode FT-ICR MS, Analytical Chemistry, 83, 4193-4199,
870 https://doi.org/10.1021/ac200464q, 2011.

871 Bai, D. P., Wang, H. L., Tan, Y., Yin, Y., Wu, Z. J., Guo, S., Shen, L. J., Zhu, B.,
872 Wang, J. H., and Kong, X. C.: Optical properties of aerosols and chemical composition
873 apportionment under different pollution levels in Wuhan during January 2018,
874 https://doi.org/10.3390/atmos11010017, 2020.

875 Barsotti, F., Ghigo, G., and Vione, D.: Computational assessment of the
876 fluorescence emission of phenol oligomers: A possible insight into the fluorescence
877 properties of humic-like substances (HULIS), J. Photochem. Photobiol., A, 315, 87-93,
878 https://doi.org/10.1016/j.jphotochem.2015.09.012, 2016.

879 Birdwell, J. E. and Engel, A. S.: Characterization of dissolved organic matter in
880 cave and spring waters using UV–Vis absorbance and fluorescence spectroscopy, Org.
881 Geochem., 41, 270-280, https://doi.org/10.1016/j.orggeochem.2009.11.002, 2010.

882 Bond, T. C. and Bergstrom, R. W.: Light absorption by carbonaceous particles: an

883   investigative   review,   Aerosol   Sci.   Technol.,   40,   27-67,

884   https://doi.org/10.1080/02786820500421521, 2006.

885   Bones, D. L., Henricksen, D. K., Mang, S. A., Gonsior, M., Bateman, A. P.,

886   Nguyen, T. B., Cooper, W. J., and Nizkorodov, S. A.: Appearance of strong absorbers

887   and fluorophores in limonene-O3 secondary organic aerosol due to NH4+-mediated

888   chemical   aging   over   long   time   scales,   J.   Geophys.   Res.:   Atmos.,   115,

889   https://doi.org/10.1029/2009JD012864, 2010.

890   Bozzetti, C., El Haddad, I., Salameh, D., Daellenbach, K. R., Fermo, P., Gonzalez,

891   R., Minguillón, M. C., Iinuma, Y., Poulain, L., Elser, M., Müller, E., Slowik, J. G.,

892   Jaffrezo, J. L., Baltensperger, U., Marchand, N., and Prévôt, A. S. H.: Organic aerosol

893   source apportionment by offline-AMS over a full year in Marseille, Atmos. Chem.

894   Phys., 17, 8247-8268, https://doi.org/10.5194/acp-17-8247-2017, 2017.

895   Budisulistiorini, S. H., Riva, M., Williams, M., Chen, J., Itoh, M., Surratt, J. D.,

896   and Kuwata, M.: Light-absorbing brown carbon aerosol constituents from combustion

897   of   indonesian   peat   and   biomass,   Environ.   Sci.   Technol.,   51,   4415-4423,

898   https://doi.org/10.1021/acs.est.7b00397, 2017.

899   Cain, J., Laskin, A., Kholghy, M. R., Thomson, M. J., and Wang, H.: Molecular

900   characterization of organic content of soot along the centerline of a coflow diffusion

901   flame,   Phys.   Chem.   Chem.   Phys.,   16,   25862-25875,

902   https://doi.org/10.1039/C4CP03330B, 2014.

903   Canagaratna, M. R., Jayne, J. T., Ghertner, D. A., Herndon, S., Shi, Q., Jimenez, J.

904   L., Silva, P. J., Williams, P., Lanni, T., Drewnick, F., Demerjian, K. L., Kolb, C. E., and

905   Worsnop, D. R.: Chase studies of particulate emissions from in-use New York City

906   vehicles,   Aerosol   Sci.   Technol.,   38,   555-573,

907   https://doi.org/10.1080/02786820490465504, 2004.

908   Canagaratna, M. R., Jimenez, J. L., Kroll, J. H., Chen, Q., Kessler, S. H., Massoli,

909   P., Hildebrandt Ruiz, L., Fortner, E., Williams, L. R., Wilson, K. R., Surratt, J. D.,

910   Donahue, N. M., Jayne, J. T., and Worsnop, D. R.: Elemental ratio measurements of

911   organic compounds using aerosol mass spectrometry: characterization, improved

912   calibration,   and   implications,   Atmos.   Chem.   Phys.,   15,   253-272,

913   https://doi.org/10.5194/acp-15-253-2015, 2015.

914   Cao, T., Li, M. J., Zou, C. L., Fan, X. J., Song, J. Z., Jia, W. L., Yu, C. L., Yu, Z.

915   Q., and Peng, P. A.: Chemical composition, optical properties, and oxidative potential

916   of water- and methanol-soluble organic compounds emitted from the combustion of

917   biomass   materials   and   coal,   Atmos.   Chem.   Phys.,   21,   13187-13205,

918   https://doi.org/10.5194/acp-21-13187-2021, 2021.

919   Cavalli, F., Facchini, M. C., Decesari, S., Mircea, M., Emblico, L., Fuzzi, S.,

920   Ceburnis, D., Yoon, Y. J., O'Dowd, C. D., Putaud, J. P., and Dell'Acqua, A.: Advances

921   in characterization of size-resolved organic matter in marine aerosol over the North

922   Atlantic, J. Geophys. Res.: Atmos., 109, https://doi.org/10.1029/2004JD005137, 2004.

923   Chakrabarty, R. K., Moosmüller, H., Chen, L. W. A., Lewis, K., Arnott, W. P.,

924   Mazzoleni, C., Dubey, M. K., Wold, C. E., Hao, W. M., and Kreidenweis, S. M.: Brown

925   carbon in tar balls from smoldering biomass combustion, Atmos. Chem. Phys., 10,

926   6363-6370, https://doi.org/10.5194/acp-10-6363-2010, 2010.

927   Chen, K. P., Raeofy, N., Lum, M., Mayorga, R., Woods, M., Bahreini, R., Zhang,

928   H. F., and Lin, Y. H.: Solvent effects on chemical composition and optical properties of

929   extracted secondary brown carbon constituents, Aerosol Sci. Technol., 56, 917-930,

930   https://doi.org/10.1080/02786826.2022.2100734, 2022.

931   Chen, Q. C., Hua, X. Y., Li, J. W., Chang, T., and Wang, Y. Q.: Diurnal evolutions

932   and sources of water-soluble chromophoric aerosols over Xi'an during haze event, in

933   Northwest   China,   Sci.   Total   Environ.,   786,   147412,

934   https://doi.org/10.1016/j.scitotenv.2021.147412, 2021.

935   Chen, Q. C., Li, J. W., Hua, X. Y., Jiang, X. T., Mu, Z., Wang, M. M., Wang, J.,

936   Shan, M., Yang, X. D., Fan, X. J., Song, J. Z., Wang, Y. Q., Guan, D. J., and Du, L.:

937   Identification of species and sources of atmospheric chromophores by fluorescence

938   excitation-emission matrix with parallel factor analysis, Sci. Total Environ., 718,

939   137322, https://doi.org/10.1016/j.scitotenv.2020.137322, 2020a.

940   Chen, Q. C., Miyazaki, Y., Kawamura, K., Matsumoto, K., Coburn, S., Volkamer,

941 R., Iwamoto, Y., Kagami, S., Deng, Y. G., Ogawa, S. H., Ramasamy, S., Kato, S., Ida,

942 A., Kajii, Y., and Mochida, M.: Characterization of chromophoric water-soluble organic

943 matter in urban, forest, and marine aerosols by HR-ToF-AMS analysis and excitation–

944 emission matrix spectroscopy, Environ. Sci. Technol., 50, 10351-10360,

945 https://doi.org/10.1021/acs.est.6b01643, 2016.

946   Chen, Y. and Bond, T. C.: Light absorption by organic carbon from wood

947 combustion, Atmos. Chem. Phys., 10, 1773-1787, https://doi.org/10.5194/acp-10-

948 1773-2010, 2010.

949   Chen, Y. F., Ge, X. L., Chen, H., Xie, X. C., Chen, Y. T., Wang, J. F., Ye, Z. L.,

950 Bao, M. Y., Zhang, Y. L., and Chen, M. D.: Seasonal light absorption properties of

951 water-soluble brown carbon in atmospheric fine particles in Nanjing, China, Atmos.

952 Environ., 187, 230-240, https://doi.org/10.1016/j.atmosenv.2018.06.002, 2018.

953   Chen, Y. F., Xie, X. C., Shi, Z., Li, Y. L., Gai, X. Y., Wang, J. F., Li, H. W., Wu, Y.,

954 Zhao, X. Y., Chen, M. D., and Ge, X. L.: Brown carbon in atmospheric fine particles in

955 Yangzhou, China: Light absorption properties and source apportionment, Atmos. Res.,

956 244, 105028, https://doi.org/10.1016/j.atmosres.2020.105028, 2020b.

957   Cheng, Y., He, K. B., Du, Z. Y., Engling, G., Liu, J. M., Ma, Y. L., Zheng, M., and

958 Weber, R. J.: The characteristics of brown carbon aerosol during winter in Beijing,

959 Atmos. Environ., 127, 355-364, https://doi.org/10.1016/j.atmosenv.2015.12.035, 2016.

960   Coble, P. G.: Characterization of marine and terrestrial DOM in seawater using

961 excitation-emission matrix spectroscopy, Mar. Chem., 51, 325-346,

962 https://doi.org/10.1016/0304-4203(95)00062-3, 1996.

963   Deng, J. J., Ma, H., Wang, X. F., Zhong, S. J., Zhang, Z. M., Zhu, J. L., Fan, Y. B.,

964 Hu, W., Wu, L. B., Li, X. D., Ren, L. J., Pavuluri, C. M., Pan, X. L., Sun, Y. L., Wang,

965 Z. F., Kawamura, K., and Fu, P. Q.: Measurement report: Optical properties and sources

966 of water-soluble brown carbon in Tianjin, North China – insights from organic

967 molecular compositions, Atmos. Chem. Phys., 22, 6449-6470,

968 https://doi.org/10.5194/acp-22-6449-2022, 2022.

969   Dey, S., Mukherjee, A., Polana, A. J., Rana, A., Mao, J. Y., Jia, S. G., Yadav, A. K.,

970   Khillare, P. S., and Sarkar, S.: Brown carbon aerosols in the Indo-Gangetic Plain

971   outflow: insights from excitation emission matrix (EEM) fluorescence spectroscopy,

972   Environ. Sci.: Processes Impacts, 23, 745-755, https://doi.org/10.1039/D1EM00050K,

973   2021.

974   Dong, W. M., Wan, J. M., Tokunaga, T. K., Gilbert, B., and Williams, K. H.:

975   Transport and humification of dissolved organic matter within a semi-arid floodplain,

976   J. Environ. Sci, 57, 24-32, https://doi.org/10.1016/j.jes.2016.12.011, 2017.

977   Dührkop, K., Fleischauer, M., Ludwig, M., Aksenov, A. r. A., Melnik, A. V.,

978   Meusel, M., Dorrestein, P. r. C., Rousu, J., and Böcker, S.: SIRIUS 4: a rapid tool for

979   turning tandem mass spectra into metabolite structure information, Nat. Methods, 16,

980   299-302, https://doi.org/10.1038/s41592-019-0344-8, 2019.

981   Fan, X. J., Wei, S. Y., Zhu, M. B., Song, J. Z., and Peng, P. A.: Comprehensive

982   characterization of humic-like substances in smoke PM2.5 emitted from the combustion

983   of biomass materials and fossil fuels, Atmos. Chem. Phys., 16, 13321-13340,

984   https://doi.org/10.5194/acp-16-13321-2016, 2016.

985   Fan, X. J., Yu, X. F., Wang, Y., Xiao, X., Li, F. Y., Xie, Y., Wei, S. Y., Song, J. Z.,

986   and Peng, P. A.: The aging behaviors of chromophoric biomass burning brown carbon

987   during dark aqueous hydroxyl radical oxidation processes in laboratory studies, Atmos.

988   Environ., 205, 9-18, https://doi.org/10.1016/j.atmosenv.2019.02.039, 2019.

989   Fasola, S., Maio, S., Baldacci, S., La Grutta, S., Ferrante, G., Forastiere, F.,

990   Stafoggia, M., Gariazzo, C., and Viegi, G.: Effects of particulate matter on the incidence

991   of respiratory diseases in the pisan longitudinal study, Int. J. Environ. Res. Public Health,

992   17, https://doi.org/10.3390/ijerph17072540, 2020.

993   Feng, Y., Ramanathan, V., and Kotamarthi, V. R.: Brown carbon: a significant

994   atmospheric absorber of solar radiation?, Atmos. Chem. Phys., 13, 8607-8621,

995   https://doi.org/10.5194/acp-13-8607-2013, 2013.

996   Fleming, L. T., Lin, P., Roberts, J. M., Selimovic, V., Yokelson, R., Laskin, J.,

997   Laskin, A., and Nizkorodov, S. A.: Molecular composition and photochemical lifetimes

998   of brown carbon chromophores in biomass burning organic aerosol, Atmos. Chem.

999   Phys., 20, 1105-1129, https://doi.org/10.5194/acp-20-1105-2020, 2020.

1000   Fu, P. Q., Kawamura, K., Chen, J., Qin, M. Y., Ren, L. J., Sun, Y. L., Wang, Z. F.,
1001   Barrie, L. A., Tachibana, E., Ding, A. J., and Yamashita, Y.: Fluorescent water-soluble
1002   organic aerosols in the High Arctic atmosphere, Sci. Rep., 5, 9845,
1003   https://doi.org/10.1038/srep09845, 2015.

1004   Ge, X. L., Wexler, A. S., and Clegg, S. L.: Atmospheric amines – part I. a review,
1005   Atmos. Environ., 45, 524-546, https://doi.org/10.1016/j.atmosenv.2010.10.012, 2011.

1006   Ge, X. L., Sun, Y. L., Trousdell, J., Chen, M. D., and Zhang, Q.: Enhancing
1007   characterization of organic nitrogen components in aerosols and droplets using high-
1008   resolution aerosol mass spectrometry, Atmos. Meas. Tech., 17, 423-439,
1009   https://doi.org/10.5194/amt-17-423-2024, 2024.

1010   Ge, X. L., Li, L., Chen, Y. F., Chen, H., Wu, D., Wang, J. F., Xie, X. C., Ge, S., Ye,
1011   Z. L., Xu, J. Z., and Chen, M. D.: Aerosol characteristics and sources in Yangzhou,
1012   China resolved by offline aerosol mass spectrometry and other techniques, Environ.
1013   Pollut., 225, 74-85, https://doi.org/10.1016/j.envpol.2017.03.044, 2017.

1014   Gilardoni, S., Massoli, P., Paglione, M., Giulianelli, L., Carbone, C., Rinaldi, M.,
1015   Decesari, S., Sandrini, S., Costabile, F., Gobbi, G. P., Pietrogrande, M. C., Visentin, M.,
1016   Scotto, F., Fuzzi, S., and Facchini, M. C.: Direct observation of aqueous secondary
1017   organic aerosol from biomass-burning emissions, Proc. Natl. Acad. Sci. U. S. A., 113,
1018   10013-10018, https://doi.org/10.1073/pnas.1602212113, 2016.

1019   González, C., Mira-M., J., and Juárez, I.: Important variable assessment and
1020   electricity price forecasting based on regression tree models: classification and
1021   regression trees, Bagging and Random Forests, IET Gener. Transm. Dis., 9, 1120-1128,
1022   https://doi.org/10.1049/iet-gtd.2014.0655, 2015.

1023   Gu, C. J., Cui, S. J., Ge, X. L., Wang, Z. Y., Chen, M. J., Qian, Z. H., Liu, Z. Y.,
1024   Wang, X. F., and Zhang, Y. J.: Chemical composition, sources and optical properties of
1025   nitrated aromatic compounds in fine particulate matter during winter foggy days in
1026   Nanjing, China, Environ. Res., 212, 113255,
1027   https://doi.org/10.1016/j.envres.2022.113255, 2022.

1028   Hawkins, L. N., Lemire, A. N., Galloway, M. M., Corrigan, A. L., Turley, J. J.,

1029 Espelien, B. M., and De H., D. O.: Maillard chemistry in clouds and aqueous aerosol

1030 as a source of atmospheric humic-like substances, Environ. Sci. Technol., 50, 7443-

1031 7452, https://doi.org/10.1021/acs.est.6b00909, 2016.

1032   Hecobian, A., Zhang, X., Zheng, M., Frank, N., Edgerton, E. S., and Weber, R. J.:

1033 Water-soluble organic aerosol material and the light-absorption characteristics of

1034 aqueous extracts measured over the southeastern united states, Atmos. Chem. Phys., 10,

1035 5965-5977, https://doi.org/10.5194/acp-10-5965-2010, 2010.

1036   Hu, J. L., Wang, P., Ying, Q., Zhang, H. L., Chen, J. J., Ge, X. L., Li, X. H., Jiang,

1037 J. K., Wang, S. X., Zhang, J., Zhao, Y., and Zhang, Y. Y.: Modeling biogenic and

1038 anthropogenic secondary organic aerosol in China, Atmos. Chem. Phys., 17, 77-92,

1039 https://doi.org/10.5194/acp-17-77-2017, 2017.

1040   Huang, L. B., Liu, T. S., and Grassian, V. i. H.: Radical-Initiated formation of

1041 aromatic organosulfates and sulfonates in the aqueous phase, Environ. Sci. Technol.,

1042 54, 11857-11864, https://doi.org/10.1021/acs.est.0c05644, 2020.

1043   Huang, R. J., Yang, L., Shen, J. C., Yuan, W., Gong, Y. Q., Ni, H. Y., Duan, J., Yan,

1044 J., Huang, H. B., You, Q. H., and Li, Y., J.: Chromophoric fingerprinting of brown

1045 carbon from residential biomass burning, Environ. Sci. Technol. Lett., 9, 102-111,

1046 https://doi.org/10.1021/acs.estlett.1c00837, 2022.

1047   Huang, R. J., Yang, L., Cao, J. J., Chen, Y., Chen, Q., Li, Y. J., Duan, J., Zhu, C.

1048 S., Dai, W. T., Wang, K., Lin, C. S., Ni, H. Y., Corbin, J. C., Wu, Y. F., Zhang, R. J., Tie,

1049 X. X., Hoffmann, T., O'Dowd, C., and Dusek, U.: Brown carbon aerosol in urban Xi'

1050 an, northwest China: the composition and light absorption properties, Environ. Sci.

1051 Technol., 52, 6825-6833, https://doi.org/10.1021/acs.est.8b02386, 2018.

1052   Huguet, A., Vacher, L., Relexans, S., Saubusse, S., Froidefond, J. M., and Parlanti,

1053 E.: Properties of fluorescent dissolved organic matter in the Gironde Estuary, Org.

1054 Geochem., 40, 706-719, https://doi.org/10.1016/j.orggeochem.2009.03.002, 2009.

1055   Jaoui, M., Corse, E., Kleindienst, T. E., Offenberg, J. H., Lewandowski, M., and

1056 Edney, E. O.: Analysis of secondary organic aerosol compounds from the

1057   photooxidation of d-limonene in the presence of NOX and their detection in ambient

1058   PM2.5, Environ. Sci. Technol., 40, 3819-3828, https://doi.org/10.1021/es052566z,

1059   2006.

1060   Jiang, W. Q., Misovich, M. V., Hettiyadura, A. P. S., Laskin, A., McFall, A. S.,

1061   Anastasio, C., and Zhang, Q.: Photosensitized Reactions of a phenolic carbonyl from

1062   wood combustion in the aqueous phase—chemical evolution and light absorption

1063   properties   of   aqSOA,   Environ.   Sci.   Technol.,   55,   5199-5211,

1064   https://doi.org/10.1021/acs.est.0c07581, 2021.

1065   Jiang, X. T., Liu, D. T., Li, Q., Tian, P., Wu, Y. Z., Li, S. Y., Hu, K., Ding, S., Bi,

1066   K., Li, R. J., Huang, M. Y., Ding, D. P., Chen, Q. C., Kong, S. F., Li, W. J., Pang, Y.,

1067   and He, D.: Connecting the light absorption of atmospheric organic aerosols with

1068   oxidation   state   and   polarity,   Environ.   Sci.   Technol.,   56,   12873-12885,

1069   https://doi.org/10.1021/acs.est.2c02202, 2022.

1070   Jo, D. S., Park, R. J., Lee, S., Kim, S. W., and Zhang, X.: A global simulation of

1071   brown carbon: implications for photochemistry and direct radiative effect, Atmos.

1072   Chem. Phys., 16, 3413-3432, https://doi.org/10.5194/acp-16-3413-2016, 2016.

1073   Kim, H. J., Collier, S., Ge, X. L., Xu, J. Z., Sun, Y. L., Jiang, W. Q., Wang, Y. L.,

1074   Herckes, P., and Zhang, Q.: Chemical processing of water-soluble species and

1075   formation of secondary organic aerosol in fogs, Atmos. Environ., 200, 158-166,

1076   https://doi.org/10.1016/j.atmosenv.2018.11.062, 2019.

1077   Kourtchev, I., O'Connor, I. P., Giorio, C., Fuller, S. J., Kristensen, K., Maenhaut,

1078   W., Wenger, J. C., Sodeau, J. R., Glasius, M., and Kalberer, M.: Effects of

1079   anthropogenic emissions on the molecular composition of urban organic aerosols: An

1080   ultrahigh resolution mass spectrometry study, Atmos. Environ., 89, 525-532,

1081   https://doi.org/10.1016/j.atmosenv.2014.02.051, 2014.

1082   Kroll, J. H., Donahue, N. M., Jimenez, J. L., Kessler, S. H., Canagaratna, M. R.,

1083   Wilson, K. R., Altieri, K. E., Mazzoleni, L. R., Wozniak, A. S., Bluhm, H., Mysak, E.

1084   R., Smith, J. D., Kolb, C. E., and Worsnop, D. R.: Carbon oxidation state as a metric

1085   for describing the chemistry of atmospheric organic aerosol, Nat. Chem., 3, 133-139,

1086   https://doi.org/10.1038/nchem.948, 2011.

1087   Kuang, Y., Shang, J., and Chen, Q. C.: Effect of ozone aging on light absorption

1088   and fluorescence of brown carbon in soot particles: The important role of polycyclic

1089   aromatic   hydrocarbons,   J.   Hazard.   Mater.,   413,   125406,

1090   https://doi.org/10.1016/j.jhazmat.2021.125406, 2021.

1091   Kuang, Y., Shang, J., Sheng, M. S., Shi, X. D., Zhu, J. L., and Qiu, X. H.:

1092   Molecular Composition of Beijing PM(2.5) Brown Carbon Revealed by an Untargeted

1093   Approach Based on Gas Chromatography and Time-of-Flight Mass Spectrometry,

1094   Environ. Sci. Technol., 57, 909-919, https://doi.org/10.1021/acs.est.2c05918, 2023.

1095   Kumar, V., Giannoukos, S., Haslett, S. L., Tong, Y., Singh, A., Bertrand, A., Lee,

1096   C. P., Wang, D. S., Bhattu, D., Stefenelli, G., Dave, J. S., Puthussery, J. V., Qi, L., Vats,

1097   P., Rai, P., Casotto, R., Satish, R., Mishra, S., Pospisilova, V., Mohr, C., Bell, D. M.,

1098   Ganguly, D., Verma, V., Rastogi, N., Baltensperger, U., Tripathi, S. N., Prévôt, A. S. H.,

1099   and Slowik, J. G.: Highly time-resolved chemical speciation and source apportionment

1100   of organic aerosol components in Delhi, India, using extractive electrospray ionization

1101   mass spectrometry, Atmos. Chem. Phys., 22, 7739-7761, https://10.5194/acp-22-7739-

1102   2022, 2022.

1103   Laskin, A., Laskin, J., and Nizkorodov, S. A.: Chemistry of atmospheric brown

1104   carbon, Chem. Rev., 115, 4335-4382, https://doi.org/10.1021/cr5006167, 2015.

1105   Laskin, A., Smith, J. S., and Laskin, J.: Molecular characterization of nitrogen-

1106   containing organic compounds in biomass burning aerosols using high-resolution mass

1107   spectrometry,   Environ.   Sci.   Technol.,   43,   3764-3771,

1108   https://doi.org/10.1021/es803456n, 2009.

1109   Lee, H. L., Laskin, A., Laskin, J., and Nizkorodov, S. A.: Excitation–emission

1110   spectra and fluorescence quantum yields for fresh and aged biogenic secondary organic

1111   aerosols, Environ. Sci. Technol., 47, 5763-5770, https://doi.org/10.1021/es400644c,

1112   2013.

1113   Li, H., Qin, X. F., Wang, G. C., Xu, J., Wang, Lu, D., Liu, C., Zheng, H., Liu, J.

1114   G., Huang, K., and Deng, C. R.: Conjoint impacts of continental outflows and marine

1115 sources on brown carbon in the East China sea: Abundances, optical properties, and

1116 formation processes, Atmos. Environ., 273, 118959,

1117 https://doi.org/10.1016/j.atmosenv.2022.118959, 2022.

1118 Li, H. W., Cui, L., Huang, Y., Zhang, Y. J., Wang, J. F., Chen, M. D., and Ge, X.

1119 L.: Concurrent dominant pathways of multifunctional products formed from nocturnal

1120 isoprene oxidation, Chemosphere, 322, 138185,

1121 https://doi.org/10.1016/j.chemosphere.2023.138185, 2023.

1122 Li, M., Wang, X. F., Lu, C. Y., Li, R., Zhang, J., Dong, S. W., Yang, L. X., Xue, L.,

1123 Chen, J. M., and Wang, W. X.: Nitrated phenols and the phenolic precursors in the

1124 atmosphere in urban Jinan, China, Sci. Total Environ., 714, 136760,

1125 https://doi.org/10.1016/j.scitotenv.2020.136760, 2020.

1126 Li, M. J., Fan, X. J., Zhu, M. B., Zou, C. L., Song, J. Z., Wei, S. Y., Jia, W. L., and

1127 Peng, P. A.: Abundance and light absorption properties of brown carbon emitted from

1128 residential coal combustion in China, Environ. Sci. Technol., 53, 595-603,

1129 https://doi.org/10.1021/acs.est.8b05630, 2019.

1130 Lin, G. X., Penner, J. E., Flanner, M. G., Sillman, S., Xu, L., and Zhou, C.:

1131 Radiative forcing of organic aerosol in the atmosphere and on snow: effects of SOA

1132 and brown carbon, J. Geophys. Res.: Atmos., 119, 7453-7476,

1133 https://doi.org/10.1002/2013JD021186, 2014.

1134 Lin, P., Rincon, A. G., Kalberer, M., and Yu, J. Z.: Elemental composition of

1135 HULIS in the pearl river delta region, China: results inferred from positive and negative

1136 electrospray high resolution mass spectrometric data, Environ. Sci. Technol., 46, 7454-

1137 7462, https://doi.org/10.1021/es300285d, 2012.

1138 Lin, P., Fleming, L. T., Nizkorodov, S. A., Laskin, J., and Laskin, A.:

1139 Comprehensive molecular characterization of atmospheric brown carbon by high

1140 resolution mass spectrometry with electrospray and atmospheric pressure

1141 photoionization, Anal. Chem., 90, 12493-12502,

1142 https://doi.org/10.1021/acs.analchem.8b02177, 2018.

1143 Lin, P., Bluvshtein, N., Rudich, Y., Nizkorodov, S. A., Laskin, J., and Laskin, A.:

1144   Molecular chemistry of atmospheric brown carbon inferred from a nationwide biomass

1145   burning event, Environ. Sci. Technol., 51, 11561-11570,

1146   https://doi.org/10.1021/acs.est.7b02276, 2017.

1147   Lin, P., Liu, J. M., Shilling, J. E., Kathmann, S. M., Laskin, J., and Laskin, A.:

1148   Molecular characterization of brown carbon (BrC) chromophores in secondary organic

1149   aerosol generated from photo-oxidation of toluene, Phys. Chem. Chem. Phys., 17,

1150   23312-23325, https://doi.org/10.1039/C5CP02563J, 2015.

1151   Lin, P., Aiona, P. K., Li, Y., Shiraiwa, M., Laskin, J., Nizkorodov, S. A., and Laskin,

1152   A.: Molecular characterization of brown carbon in ciomass curning aerosol particles,

1153   Environ. Sci. Technol., 50, 11815-11824, https://doi.org/10.1021/acs.est.6b03024,

1154   2016.

1155   Lobodin, V. V., Marshall, A. G., and Hsu, C. S.: Compositional space boundaries

1156   for organic compounds, Analytical Chemistry, 84, 3410-3416,

1157   https://doi.org/10.1021/ac300244f, 2012.

1158   Ma, Y. L. and Hays, M. D.: Thermal extraction – two-dimensional gas

1159   chromatography–mass spectrometry with heart-cutting for nitrogen heterocyclics in

1160   biomass burning aerosols, J. Chromatogr. A, 1200, 228-234,

1161   https://doi.org/10.1016/j.chroma.2008.05.078, 2008.

1162   Mao, J. F., Cheng, Y., Bai, Z., Zhang, W., Zhang, L. Y., Chen, H., Wang, L. N., Li,

1163   L., and Chen, J. M.: Molecular characterization of nitrogen-containing organic

1164   compounds in the winter North China Plain, Sci Total Environ, 838, 156189,

1165   https://10.1016/j.scitotenv.2022.156189, 2022.

1166   Matos, J. T. V., Freire, S. M. S. C., Duarte, R. M. B. O., and Duarte, A. C.: Natural

1167   organic matter in urban aerosols: comparison between water and alkaline soluble

1168   components using excitation–emission matrix fluorescence spectroscopy and multiway

1169   data analysis, Atmos. Environ., 102, 1-10,

1170   https://doi.org/10.1016/j.atmosenv.2014.11.042, 2015.

1171   McKnight, D. M., Boyer, E. W., Westerhoff, P. K., Doran, P. T., Kulbe, T., and

1172   Andersen, D. T.: Spectrofluorometric characterization of dissolved organic matter for

1173   indication of precursor organic material and aromaticity, Limnol. Oceanogr., 46, 38-48,

1174   https://doi.org/10.4319/lo.2001.46.1.0038, 2001.

1175   McNeill, V. F.: Aqueous organic chemistry in the atmosphere: sources and

1176   chemical processing of organic aerosols, Environ. Sci. Technol., 49, 1237-1244,

1177   https://doi.org/10.1021/es5043707, 2015.

1178   Murphy, K. R., Stedmon, C. A., Graeber, D., and Bro, R.: Fluorescence

1179   spectroscopy and multi-way techniques. PARAFAC, Anal. Methods, 5,

1180   https://doi.org/10.1039/c3ay41160e, 2013.

1181   Murphy, K. R., Hambly, A., Singh, S., Henderson, R. K., Baker, A., Stuetz, R., and

1182   Khan, S. J.: Organic matter fluorescence in municipal water recycling schemes: toward

1183   a unified PARAFAC model, Environ. Sci. Technol., 45, 2909-2916,

1184   https://doi.org/10.1021/es103015e, 2011.

1185   Negron-Encarnacion, I. and Arce, R.: Light-induced transformations of aza-

1186   aromatic pollutants adsorbed on models of atmospheric particulate matter: Acridine and

1187   9(10-H) acridone, Atmos. Environ., 41, 6771-6783,

1188   https://doi.org/10.1016/j.atmosenv.2007.04.062, 2007.

1189   Onasch, T. B., Trimborn, A., Fortner, E. C., Jayne, J. T., Kok, G. L., Williams, L.

1190   R., Davidovits, P., and Worsnop, D. R.: Soot particle aerosol mass spectrometer:

1191   development, validation, and initial application, Aerosol Sci. Technol., 46, 804-817,

1192   https://doi.org/10.1080/02786826.2012.663948, 2012.

1193   Ou, Y., Nie, D. Y., Chen, H., Ye, Z. L., and Ge, X. L.: Characterization of products

1194   from the aqueous-phase photochemical oxidation of benzene-diols, Atmosphere, 12,

1195   https://doi.org/10.3390/atmos12050534, 2021.

1196   Petters, S. S., Cui, T. Q., Zhang, Z. F., Gold, A., McNeill, V. F., Surratt, J. D., and

1197   Turpin, B. J.: Organosulfates from dark aqueous reactions of isoprene-derived

1198   epoxydiols under cloud and fog conditions: kinetics, mechanism, and effect of reaction

1199   environment on regioselectivity of sulfate addition, ACS Earth Space Chem., 5, 474-

1200   486, https://doi.org/10.1021/acsearthspacechem.0c00293, 2021.

1201   Qi, L., Chen, M. D., Stefenelli, G., Pospisilova, V., Tong, Y. D., Bertrand, A.,

1202   Hueglin, C., Ge, X. L., Baltensperger, U., Prévôt, A. S. H., and Slowik, J. G.: Organic

1203   aerosol source apportionment in Zurich using an extractive electrospray ionization

1204   time-of-flight mass spectrometer (EESI-TOF-MS) – Part 2: biomass burning

1205   influences in winter, Atmos. Chem. Phys., 19, 8037-8062, https://doi.org/10.5194/acp-

1206   19-8037-2019, 2019.

1207   Qin, J. J., Zhang, L. M., Zhou, X. M., Duan, J. C., Mu, S. T., Xiao, K., Hu, J. N.,

1208   and Tan, J. H.: Fluorescence fingerprinting properties for exploring water-soluble

1209   organic compounds in PM2.5 in an industrial city of northwest China, Atmos. Environ.,

1210   184, 203-211, https://doi.org/10.1016/j.atmosenv.2018.04.049, 2018.

1211   Qin, Y. M., Tan, H. B., Li, Y. J., Schurman, M. I., Li, F., Canonaco, F., Prévôt, A.

1212   S. H., and Chan, C. K.: Impacts of traffic emissions on atmospheric particulate nitrate

1213   and organics at a downwind site on the periphery of Guangzhou, China, Atmos. Chem.

1214   Phys., 17, 10245-10258, https://doi.org/10.5194/acp-17-10245-2017, 2017.

1215   Qiu, Y. M., Xie, Q. R., Wang, J. F., Xu, W. Q., Li, L. J., Wang, Q. Q., Zhao, J.,

1216   Chen, Y. T., Chen, Y. F., Wu, Y. Z., Du, W., Zhou, W., Lee, J., Zhao, C. F., Ge, X. L.,

1217   Fu, P. Q., Wang, Z., Worsnop, D. R., and Sun, Y. L.: Vertical characterization and source

1218   apportionment of water-soluble organic aerosol with high-resolution aerosol mass

1219   spectrometry in Beijing, China, ACS Earth Space Chem., 3, 273-284,

1220   https://doi.org/10.1021/acsearthspacechem.8b00155, 2019.

1221   Shapiro, E. L., Szprengiel, J., Sareen, N., Jen, C. N., Giordano, M. R., and McNeill,

1222   V. F.: Light-absorbing secondary organic material formed by glyoxal in aqueous aerosol

1223   mimics, Atmos. Chem. Phys., 9, 2289-2300, https://doi.org/10.5194/acp-9-2289-2009,

1224   2009.

1225   Song, J. Z., Li, M. J., Fan, X. J., Zou, C. L., Zhu, M. B., Jiang, B., Yu, Z. Q., Jia,

1226   W. L., Liao, Y. H., and Peng, P. A.: Molecular Characterization of water- and methanol-

1227   soluble organic compounds emitted from residential coal combustion using ultrahigh-

1228   resolution electrospray ionization fourier transform ion cyclotron resonance mass

1229   spectrometry, Environ. Sci. Technol., 53, 13607-13617,

1230   https://doi.org/10.1021/acs.est.9b04331, 2019.

1231   Sun, Y. L., Du, W., Fu, P. Q., Wang, Q. Q., Li, J., Ge, X. L., Zhang, Q., Zhu, C. M.,

1232   Ren, L. J., Xu, W. Q., Zhao, J., Han, T. T., Worsnop, D. R., and Wang, Z.: Primary and

1233   secondary aerosols in Beijing in winter: sources, variations and processes, Atmos.

1234   Chem. Phys., 16, 8309-8329, https://doi.org/10.5194/acp-16-8309-2016, 2016.

1235   Tang, J., Li, J., Zhao, S. Z., Zhong, G. C., Mo, Y. Z., Jiang, H. X., Jiang, B., Chen,

1236   Y. J., Tang, J. H., Tian, C. G., Zong, Z., Hussain S., J., Song, J. Z., and Zhang, G.:

1237   Molecular signatures and formation mechanisms of water-soluble chromophores in

1238   particulate matter from Karachi in Pakistan, Sci. Total Environ., 914, 169890,

1239   https://doi.org/10.1016/j.scitotenv.2024.169890, 2024.

1240   Tsugawa, H., Cajka, T., Kind, T., Ma, Y., Higgins, B., Ikeda, K., Kanazawa, M.,

1241   VanderGheynst, J., Fiehn, O., and Arita, M.: MS-DIAL: data-independent MS/MS

1242   deconvolution for comprehensive metabolome analysis, Nat. Methods, 12, 523-526,

1243   https://doi.org/10.1038/nmeth.3393, 2015.

1244   Ulbrich, I. M., Canagaratna, M. R., Zhang, Q., Worsnop, D. R., and Jimenez, J. L.:

1245   Interpretation of organic components from Positive Matrix Factorization of aerosol

1246   mass spectrometric data, Atmos. Chem. Phys., 9, 2891-2918,

1247   https://doi.org/10.5194/acp-9-2891-2009, 2009.

1248   Updyke, K. M., Nguyen, T. B., and Nizkorodov, S. A.: Formation of brown carbon

1249   via reactions of ammonia with secondary organic aerosols from biogenic and

1250   anthropogenic precursors, Atmos. Environ., 63, 22-31,

1251   https://doi.org/10.1016/j.atmosenv.2012.09.012, 2012.

1252   Wang, D. W., Shen, Z. X., Zhang, Q., Lei, Y. L., Zhang, T., Huang, S. S., Sun, J.,

1253   Xu, H. M., and Cao, J. J.: Winter brown carbon over six of China's megacities: light

1254   absorption, molecular characterization, and improved source apportionment revealed

1255   by multilayer perceptron neural network, Atmos. Chem. Phys., 22, 14893-14904,

1256   https://doi.org/10.5194/acp-22-14893-2022, 2022a.

1257   Wang, J. F., Ge, X. L., Sonya, C., Ye, J. H., Lei, Y. L., Chen, M. D., and Zhang, Q.:

Influence of regional emission controls on the chemical composition, sources, and size distributions of submicron aerosols: Insights from the 2014 Nanjing Youth Olympic Games, Sci. Total Environ., 807, 150869, https://doi.org/10.1016/j.scitotenv.2021.150869, 2022b.

Wang, J. F., Ge, X. L., Chen, Y. F., Shen, Y. F., Zhang, Q., Sun, Y. L., Xu, J. Z., Ge, S., Yu, H., and Chen, M. D.: Highly time-resolved urban aerosol characteristics during springtime in Yangtze River Delta, China: insights from soot particle aerosol mass spectrometry, Atmos. Chem. Phys., 16, 9109-9127, https://doi.org/10.5194/acp-16-9109-2016, 2016.

Wang, J. F., Ye, J. H., Zhang, Q., Zhao, J., Wu, Y. Z., Li, J. Y., Liu, D. T., Li, W. J., Zhang, Y. G., Wu, C., Xie, C. H., Qin, Y. M., Lei, Y. L., Huang, X. P., Guo, J. P., Liu, P. F., Fu, P. Q., Li, Y. J., Lee, H. C., Choi, H., Zhang, J., Liao, H., Chen, M. D., Sun, Y. L., Ge, X. L., Martin, S. T., and Jacob, D. J.: Aqueous production of secondary organic aerosol from fossil-fuel emissions in winter Beijing haze, Proc. Natl. Acad. Sci. U. S. A., 118, https://doi.org/10.1073/pnas.2022179118, 2021.

Wang, K., Zhang, Y., Huang, R. J., Cao, J. J., and Hoffmann, T.: UHPLC-Orbitrap mass spectrometric characterization of organic aerosol from a central European city (Mainz, Germany) and a Chinese megacity (Beijing), Atmos. Environ., 189, 22-29, https://doi.org/10.1016/j.atmosenv.2018.06.036, 2018a.

Wang, L. W., Wang, X. F., Gu, R. R., Wang, H., Yao, L., Wen, L., Zhu, F. P., Wang, W. H., Xue, L. K., Yang, L. X., Lu, K. D., Chen, J. M., Wang, T., Zhang, Y. H., and Wang, W. X.: Observations of fine particulate nitrated phenols in four sites in northern China: concentrations, source apportionment, and secondary formation, Atmos. Chem. Phys., 18, 4349-4359, https://doi.org/10.5194/acp-18-4349-2018, 2018b.

Wang, Y. J., Hu, M., Lin, P., Guo, Q. F., Wu, Z. J., Li, M. G., Zeng, L. M., Song, Y., Zeng, L. W., Wu, Y. S., Guo, S., Huang, X. F., and He, L. Y.: Molecular characterization of nitrogen-containing organic compounds in humic-like substances emitted from straw residue burning, Environ. Sci. Technol., 51, 5951-5961, https://doi.org/10.1021/acs.est.7b00248, 2017.

1287   Wang, Y. Q.: An open source software suite for multi-dimensional meteorological

1288   data computation and visualisation, Journal of Open Research Software, 7,

1289   https://doi.org/10.5334/jors.267, 2019.

1290   Wen, H., Zhou, Y., Xu, X. Y., Wang, T. S., Chen, Q. L., Chen, Q. C., Li, W. J.,

1291   Wang, Z., Huang, Z. W., Zhou, T., Shi, J. S., Bi, J. R., Ji, M. X., and Wang, X.: Water-

1292   soluble brown carbon in atmospheric aerosols along the transport pathway of Asian dust:

1293   Optical properties, chemical compositions, and potential sources, Sci. Total Environ.,

1294   789, 147971, https://doi.org/10.1016/j.scitotenv.2021.147971, 2021.

1295   Wu, G. M., Ram, K., Fu, P. Q., Wang, W., Zhang, Y. L., Liu, X. Y., Stone, E. A.,

1296   Pradhan, B. B., Dangol, P. M., Panday, A. K., Wan, X., Bai, Z. P., Kang, S. C., Zhang,

1297   Q. G., and Cong, Z. Y.: Water-soluble brown carbon in atmospheric aerosols from

1298   Godavari (Nepal), a regional representative of south Asia, Environ. Sci. Technol., 53,

1299   3471-3479, https://doi.org/10.1021/acs.est.9b00596, 2019a.

1300   Wu, Y. Z., Liu, D. T., Wang, J. F., Shen, F. Z., Chen, Y. F., Cui, S. J., Ge, S., Wu,

1301   Y., Chen, M. D., and Ge, X. L.: Characterization of size-resolved hygroscopicity of

1302   black carbon-containing particle in urban environment, Environ. Sci. Technol., 53,

1303   14212-14221, https://doi.org/10.1021/acs.est.9b05546, 2019b.

1304   Wu, Z., Liu, D. T., Wang, X. T., Li, S. Y., Zhang, J. L., Qiu, H., Ding, S., Hu, K.,

1305   Li, W. J., Tian, P., Liu, Q., Zhao, D. L., Ma, E. D., Chen, M. T., Xu, H. H., Ouyang, B.,

1306   Chen, Y., Kong, S. F., Ge, X. L., and Liu, H.: Ambient marine shipping emissions

1307   determined by vessel operation mode along the East China Sea, Sci. Total Environ., 769,

1308   144713, https://doi.org/10.1016/j.scitotenv.2020.144713, 2021.

1309   Xian, J. K., Cui, S. J., Chen, X. Z., Wang, J. Y., Xiong, Y. F., Gu, C. J., Wang, Y.,

1310   Zhang, Y. J., Li, H. W., Wang, J. F., and Ge, X. L.: Online chemical characterization of

1311   atmospheric fine secondary aerosols and organic nitrates in summer Nanjing, China,

1312   Atmos. Res., 290, 106783, https://doi.org/10.1016/j.atmosres.2023.106783, 2023.

1313   Xie, M. J., Mladenov, N., Williams, M. W., Neff, J. C., Wasswa, J., and Hannigan,

1314   M. P.: Water soluble organic aerosols in the Colorado Rocky Mountains, USA:

1315   composition, sources and optical properties, Sci. Rep., 6, 39339,

1316   https://doi.org/10.1038/srep39339, 2016.

1317   Xie, X. C., Chen, Y. F., Nie, D. Y., Liu, Y., Liu, Y., Lei, R. Y., Zhao, X. Y., Li, H.

1318   W., and Ge, X. L.: Light-absorbing and fluorescent properties of atmospheric brown

1319   carbon: A case study in Nanjing, China, Chemosphere, 251, 126350,

1320   https://doi.org/10.1016/j.chemosphere.2020.126350, 2020.

1321   Xing, C., Wan, Y. B., Wang, Q. Q., Kong, S. F., Huang, X. P., Ge, X. L., Xie, M.

1322   J., and Yu, H.: Molecular Characterization of Brown Carbon Chromophores in

1323   Atmospherically Relevant Samples and Their Gas-Particle Distribution and Diurnal

1324   Variation in the Atmosphere, J. Geophys. Res.: Atmos., 128, e2022JD038142,

1325   https://doi.org/10.1029/2022JD038142, 2023.

1326   Yan, G. and Kim, G.: Speciation and sources of brown carbon in precipitation at

1327   seoul, Korea: insights from excitation – emission matrix spectroscopy and carbon

1328   isotopic   analysis,   Environ.   Sci.   Technol.,   51,   11580-11587,

1329   https://doi.org/10.1021/acs.est.7b02892, 2017.

1330   Yan, J. P., Wang, X. P., Gong, P., Wang, C. F., and Cong, Z. Y.: Review of brown

1331   carbon aerosols: recent progress and perspectives, Sci. Total Environ., 634, 1475-1485,

1332   https://doi.org/10.1016/j.scitotenv.2018.04.083, 2018.

1333   Yassine, M. M., Harir, M., Dabek-Z., E., and Schmitt-K., P.: Structural

1334   characterization of organic aerosol using Fourier transform ion cyclotron resonance

1335   mass spectrometry: Aromaticity equivalent approach, Rapid Commun. Mass Spectrom.,

1336   28, 2445-2454, https://doi.org/doi.org/10.1002/rcm.7038, 2014.

1337   Ye, Z. L., Qu, Z. X., Ma, S. S., and Gai, X. L.: Secondary organic aerosols from

1338   aqueousreaction   of   aerosol   water,   Environ.   Sci.,   39(8),   3954-3964,

1339   https://doi.org/10.13227/j.hjkx.201712236, 2018.

1340   Yu, H. R., Liang, H., Qu, F. S., Han, Z. S., Shao, S. L., Chang, H. Q., and Li, G.

1341   B.: Impact of dataset diversity on accuracy and sensitivity of parallel factor analysis

1342   model of dissolved organic matter fluorescence excitation-emission matrix, Sci. Rep.,

1343   5, 10207, https://doi.org/10.1038/srep10207, 2015.

1344   Yu, J. T., Yan, C. Q., Liu, Y., Li, X. Y., Zhou, T., and Zheng, M.: Potassium: a tracer

1345   for biomass burning in Beijing?, Aerosol Air Qual. Res., 18, 2447-2459,
1346   https://doi.org/10.4209/aaqr.2017.11.0536, 2018.

1347   Zhang, B. Q., Zhang, Y. J., Zhang, K. X., Zhang, Y. C., Ji, Y., Zhu, B. Z., Liang, Z.
1348   Y., Wang, H. L., and Ge, X. L.: Machine learning assesses drivers of PM2.5 air pollution
1349   trend in the Tibetan Plateau from 2015 to 2022, Sci. Total Environ., 878, 163189,
1350   https://doi.org/10.1016/j.scitotenv.2023.163189, 2023.

1351   Zhang, Q., Jimenez, J. L., Canagaratna, M. R., Ulbrich, I. M., Ng, N. L., Worsnop,
1352   D. s. R., and Sun, Y. L.: Understanding atmospheric organic aerosols via factor analysis
1353   of aerosol mass spectrometry: a review, Anal. Bioanal. Chem., 401, 3045-3067,
1354   https://doi.org/10.1007/s00216-011-5355-y, 2011.

1355   Zhang, S. Y.: Detection of scopolamine in nori fruit juice and its traditional chinese
1356   medicine compound health products by high performance liquid chromatography,
1357   World Latest Medicine Information, 18, 91-92, https://doi.org/10.19613/j.cnki.1671-
1358   3141.2018.82.066, 2018.

1359   Zhang, X. L., Lin, Y. H., Surratt, J. D., and Weber, R. J.: Sources, composition and
1360   absorption Ångström exponent of light-absorbing organic components in aerosol
1361   extracts from the Los Angeles basin, Environ. Sci. Technol., 47, 3685-3693,
1362   https://doi.org/10.1021/es305047b, 2013.

1363   Zhang, Y. Z., Forrister, H., Liu, J. M., Dibb, J., Anderson, B., Schwarz, J. P.,
1364   Perring, A. E., Jimenez, J. L., Campuzano-Jost, P., Wang, Y. H., Nenes, A., and Weber,
1365   R. J.: Top-of-atmosphere radiative forcing affected by brown carbon in the upper
1366   troposphere, Nat. Geosci., 10, 486-489, https://doi.org/10.1038/ngeo2960, 2017.

1367   Zhong, M., Xu, J. Z., Wang, H. Q., Gao, L., Zhu, H. X., Zhai, L. X., Zhang, X. H.,
1368   and Zhao, W. H.: Characterizing water-soluble brown carbon in fine particles in four
1369   typical cities in northwestern China during wintertime: integrating optical properties
1370   with   chemical   processes,   Atmos.   Chem.   Phys.,   23,   12609-12630,
1371   https://doi.org/10.5194/acp-23-12609-2023, 2023.

1372   Zorn, S. R., Drewnick, F., Schott, M., Hoffmann, T., and Borrmann, S.:
1373   Characterization of the South Atlantic marine boundary layer aerosol using an aerodyne

1374 aerosol mass spectrometer, Atmos. Chem. Phys., 8, 4711-4728,

1375 https://doi.org/10.5194/acp-8-4711-2008, 2008.

1376 Zsolnay, A., Baigar, E., Jimenez, M., Steinweg, B., and Saccomandi, F.:

1377 Differentiating with fluorescence spectroscopy the sources of dissolved organic matter

1378 in soils subjected to drying, Chemosphere, 38, 45-50, https://doi.org/10.1016/S0045-

1379 6535(98)00166-0, 1999.

1380

1381   Table 1. The average mass concentrations of major chemical components as well as the

1382   parameters of optical properties of $PM_{2.5}$ collected in Nanjing during two seasons.

	Summer Season (SS)			Cold Season (CS)		
	Daytime	Nighttime	Average	Daytime	Nighttime	Average
OC ($\mu g\ m^{-3}$)	7.02±3.04	6.87±2.51	6.94±2.76	12.9±5.77	12.74±5.29	12.82±5.51
EC ($\mu g\ m^{-3}$)	1.13±0.31	1.22±0.37	1.17±0.34	1.94±0.93	1.6±0.74	1.77±0.86
AAE_{WSOC}	6.34±0.65	6.35±0.69	6.35±0.67	6.43±0.68	6.44±0.86	6.43±0.77
AAE_{MSOC}	6.02±0.90	5.96±0.96	5.99±0.92	7.06±0.94	6.70±0.65	6.89±0.82
WSOC ($\mu g\ m^{-3}$)	4.06±1.31	4.45±1.44	4.26±1.38	5.81±2.29	5.75±2.25	6.34±2.27
MSOC ($\mu g\ m^{-3}$)	5.64±2.12	5.79±1.89	5.72±1.99	10.42±4.98	10.49±4.57	10.45±4.75
Total ions ($\mu g\ m^{-3}$)	18.00±5.49	18.69±8.05	18.49±6.91	35.41±15.02	43.12±17.94	39.22±16.88
$Abs_{365,\ WSOC}$ ($M\ m^{-1}$)	2.15±0.90	2.38±0.80	2.27±0.85	4.89±2.63	4.86±2.46	4.87±2.53
$Abs_{365,\ MSOC}$ ($M\ m^{-1}$)	3.44±1.40	3.82±1.55	3.64±1.48	4.65±2.24	5.31±2.71	4.97±2.49
$MAE_{365,\ WSOC}$ ($m^2\ g^{-1}$)	0.54±0.16	0.56±0.15	0.55±0.16	0.73±0.20	0.77±0.21	0.75±0.21
$MAE_{365,\ MSOC}$ ($m^2\ g^{-1}$)	0.68±0.32	0.75±0.30	0.72±0.31	0.48±0.18	0.52±0.16	0.50±0.17
SFE_{WSOC} ($W\ g^{-1}$)	2.16±1.29	2.24±1.36	2.20±1.33	3.16±1.8	3.42±1.25	3.24±1.84
SFE_{MSOC} ($W\ g^{-1}$)	2.28±2.37	2.55±1.85	2.43±2.10	2.19±1.01	2.26±0.81	2.23±0.91

1383

1384   Table 2. Multi-linear regression results of the four factors and corresponding average

1385   contributions to the total light absorption of water-soluble organics (WSOA).

Factor	Coefficients ($m^2 \cdot g^{-1}$)		Contributions (%)
	Average	Standard error	
HOA	0.71	0.11	33.05
BBOA	0.71	0.06	15.49
OOA1	0.12	0.07	6.00
OOA2	0.83	0.14	45.46

1386

1387   Table 3. The average values of fluorescence indices of both water-soluble organic

1388   carbon (WSOC) and methanol-soluble organic carbon (MSOC).

	Summer Season (SS)			Cold Season (CS)		
	Day	Night	Average	Day	Night	Average
HIX_{WSOC}	3.16±0.74	3.51±1.12	3.34±0.97	4.68±0.94	4.67±0.91	4.68±0.92
HIX_{MSOC}	2.65±0.99	2.78±0.86	2.72±0.92	3.42±0.73	3.53±0.58	3.48±0.66
FI_{WSOC}	1.85±0.16	1.97±0.17	1.91±0.18	1.89±0.11	1.92±0.09	1.90±0.10
FI_{MSOC}	2.25±0.26	2.30±0.31	2.27±0.28	2.10±0.15	2.12±0.14	2.11±0.15
BIX_{WSOC}	0.81±0.16	0.86±0.14	0.84±0.15	0.86±0.10	0.91±0.08	0.88±0.09
BIX_{MSOC}	0.89±0.19	0.9±0.13	0.90±0.16	0.95±0.10	0.97±0.11	0.96±0.10

1389

1390   Table 4. The number percentages of organosulfates (OSs) in CHOS compounds in ESI⁻

1391   mode and those of nitrooxy-OSs in CHONS compounds in both modes.

	SS		CS	
	Daytime	Nighttime	Daytime	Nighttime
OSs (ESI⁻)	34.8%	42.3%	54.3%	68.6%
Nitrooxy-OSs (ESI⁻)	5.3%	12.0%	11.0%	12.5%
Nitrooxy-OSs (ESI⁺)	10.3%	11.8%	10.5%	9.8%

1392
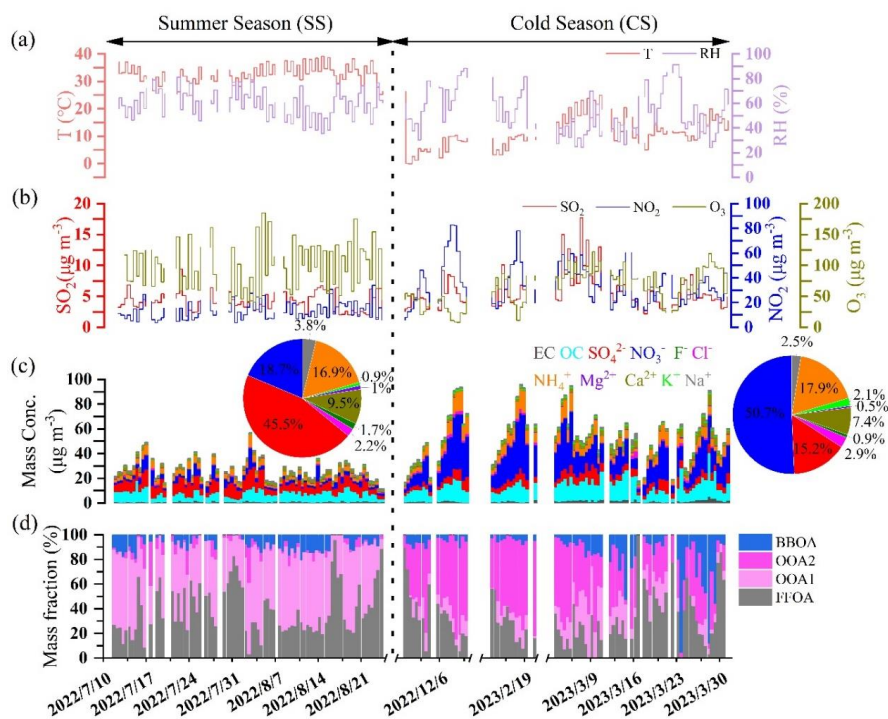
Figure 1. Time series of: (a) air temperature (T) and relative humidity (RH); (b) concentrations of nitrogen dioxide (NO_2), sulfur dioxide (SO_2) and ozone (O_3); (c) concentrations of different inorganic ions, total organic carbon (OC), and elemental carbon (EC) (two inset pies are the average mass contributions of difference ions to the total ions during SS and CS, respectively); and (d) mass percentages of different factors with respect to the total water-soluble OA
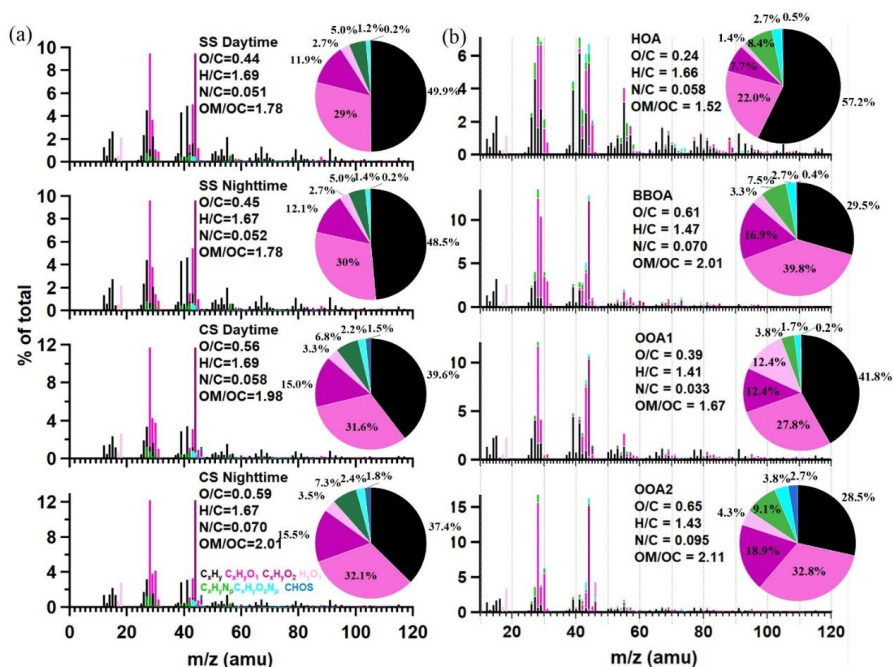
Figure 2. High-resolution mass spectra (HRMS) of (a) the water-soluble OA (WSOA) during different periods, and (b) the four resolved factors (HOA, BBOA, OOA1, OOA2). Ions are classified into and colored by different ion families, and inset pies in both charts show the mass fractional contributions of different ion families to the total HRMS correspondingly.

1407
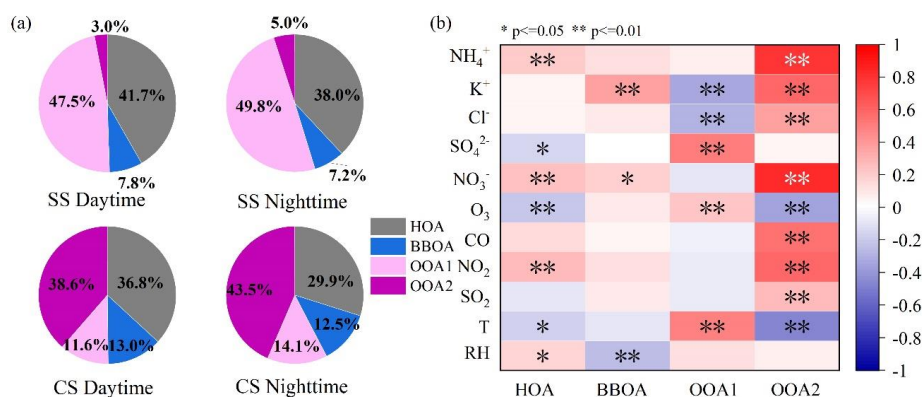
1408

Figure 3. (a) Average mass contributions of the four factor to WSOA during different periods, and (b) cross-correlation coefficients (Pearson's r) among the four factors and other aerosol components as well as gaseous species.

1409

1410

1411

1412
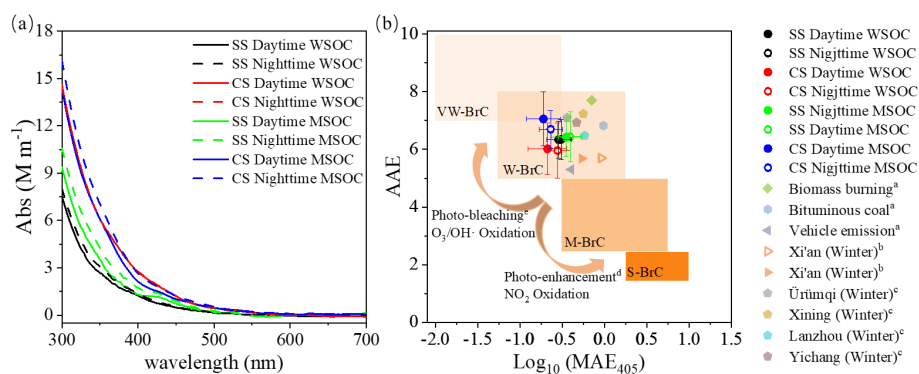
Figure 4. (a) Light absorption coefficients (Abs) of the water-soluble OC (WSOC) and methanol-soluble OC (MSOC) as a function of wavelength, and (b) distribution of the measured data in the $\log_{10}(MAE_{405})$-AAE space (Saleh, 2020)(MAE_{405}: Mass absorption efficiency at 405 nm; AAE: Absorption Ångström Exponent; The shaded areas indicate very weakly (VW), weakly (W), moderately (M), and strongly (S) absorbing brown carbon (BrC), respectively; Other markers indicate results from [a] Huang et al. (2018), [b] Chen et al. (2018) and [c] Zhong et al. (2023).
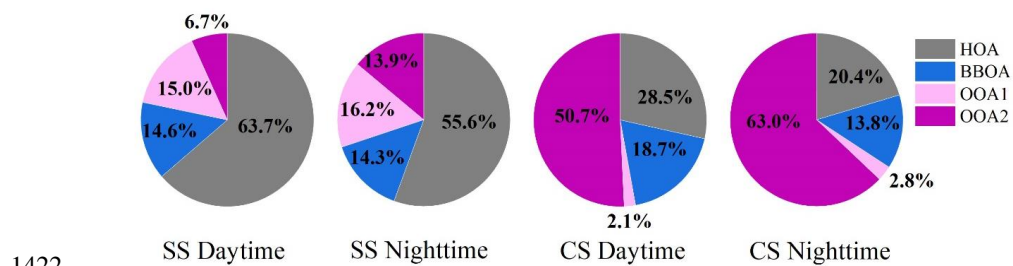
1422

1423 Figure 5. Contributions of the four factors to the total light absorption of WSOA during

1424 different periods.
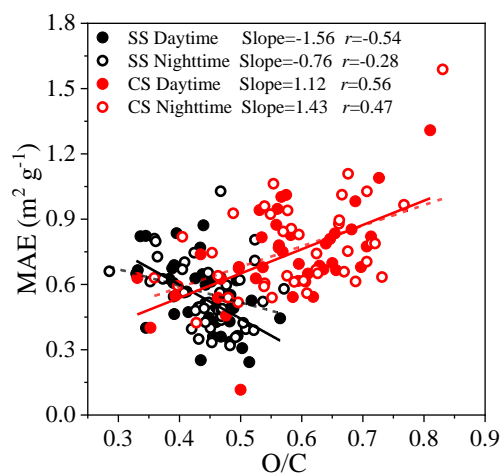
1425

1426   Figure 6. Scatter plot of MAE$_{365}$ (mass absorption efficiency at 365 nm) versus the

1427   oxygen-to-carbon (O/C) ratios for the WSOA.
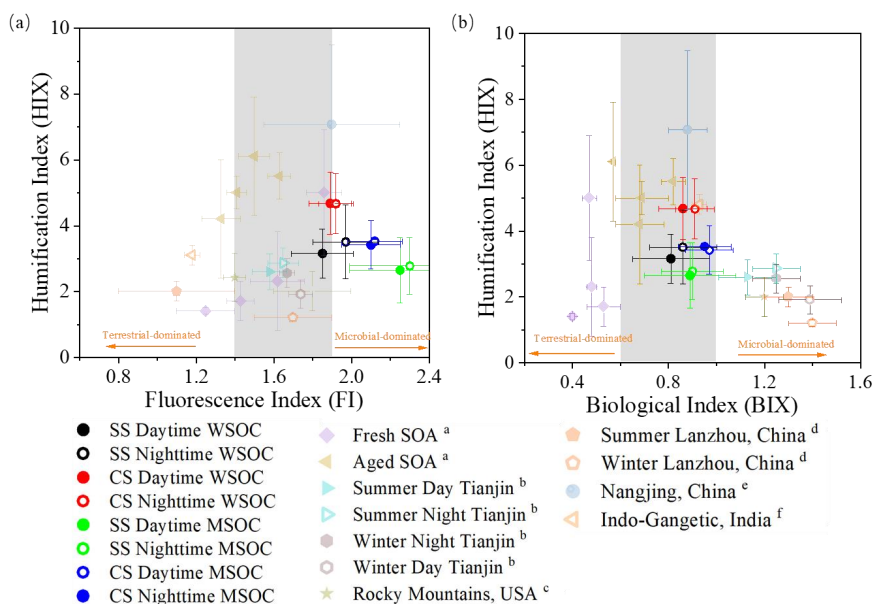
Figure 7. Distribution of the fluorescent indices of measured data in this study and a few other studies ([a] Lee et al. (2013), [b] Deng et al. (2022), [c] Xie et al. (2016), [d] Qin et al. (2018), [e] Xie et al. (2016), [f] Dey et al. (2021)): (a) Humidication index (HIX) versus fluorescenc index (FI), and (b) HIX versus biological index (BIX). The shaded areas marked 0.6 ~ 1 of BIX (Huguet et al., 2009) and 1.6 ~ 1.9 of FI (Mcknight et al., 2001).
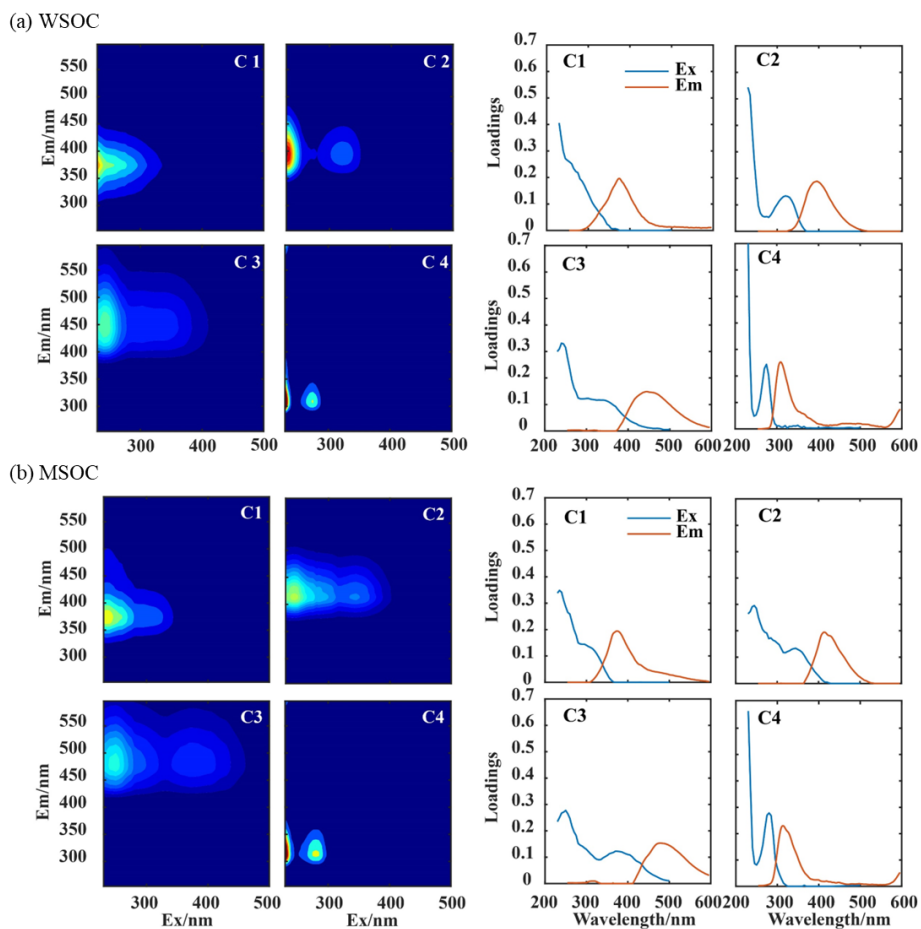
Figure 8. Four fluorescence components (C1 ~ C4) and the corresponding fluorescent intensities of emission (brown) and excitation (blue) against wavelenghth: (a) WSOC, and (b) MSOC.
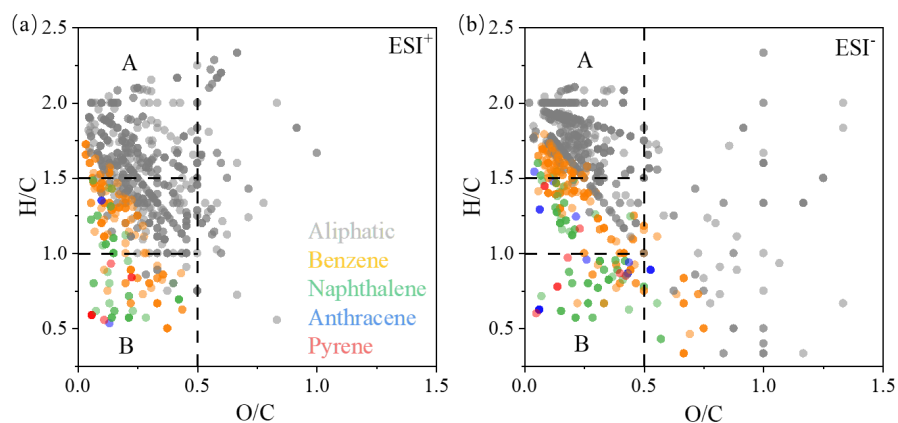
Figure 9. Van Krevelen diagram for CHO compounds detected in (a) ESI$^+$ and (b) ESI$^-$ mode. The markers with different colors represent aliphatic compounds (Xc < 2.50), aromatic benzene ring structures (2.50 ≤ Xc <2.71), naphthalene ring structures (2.71 ≤ Xc <2.80), anthracene ring structures (2.80 ≤ Xc <2.83), and pyrene ring structures (2.83 ≤ Xc <2 .92), respectively (Mao et al., 2022).
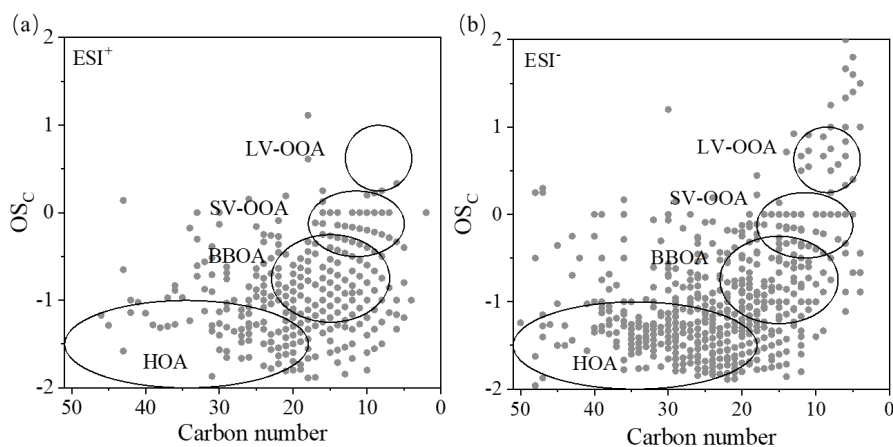
Figure 10. Scatter plots of carbon oxidation state (OSc) versus carbon number for CHO compounds: (a) ESI$^+$ mode, and (b) ESI$^-$ mode. The circled areas represent those from fossil fuel combustion hydrocarbon-like OA (HOA), biomass burning OA (BBOA), semi-volatile oxygenated OA (SV-OOA) and low-volatility oxygenated OA (LV-OOA)(Kroll et al., 2011).

1456
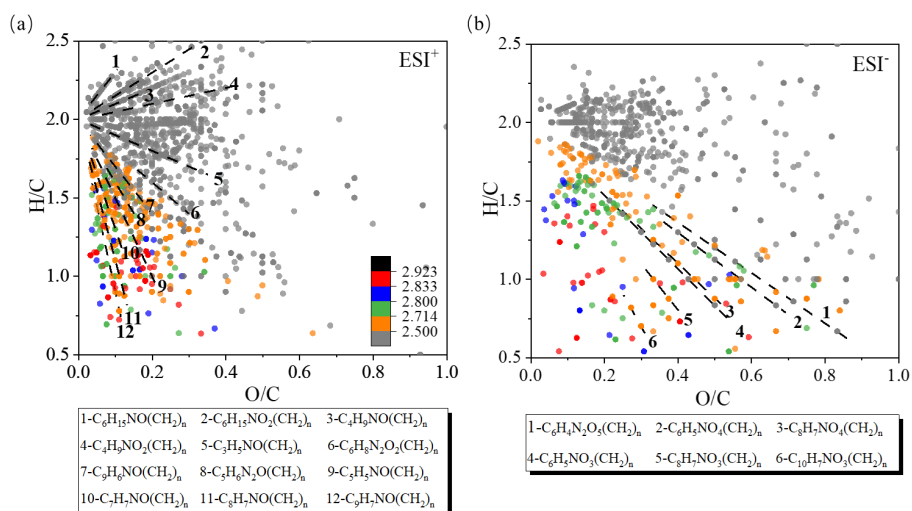
1457

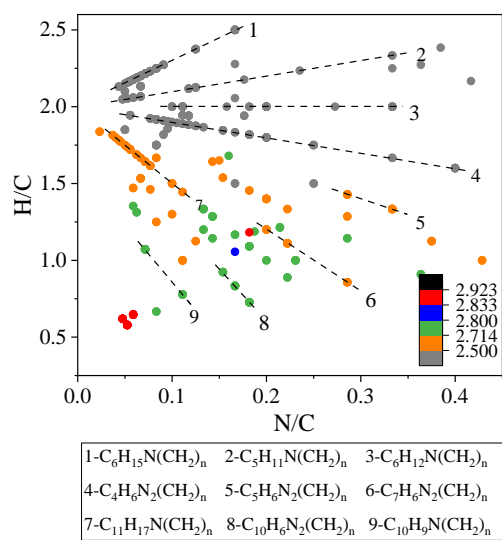Figure 11. Van Krevelen diagram for CHON compounds detected in both ESI$^+$ and ESI$^-$

mode. The data are also colored by Xc values (See caption of Fig. 9), and the different

dash lines represent different series of compounds.

1461

1462

1463
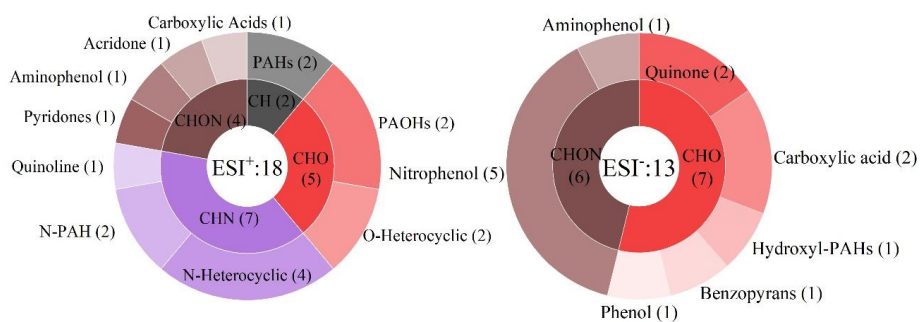
1464

Figure 12. Van Krevelen diagram of the CHN compounds in ESI[+] mode. The data are
also colored by Xc values (See caption of Fig. 9), and the different dash lines represent
different series of compounds.

1468

Figure 13. Distributions of the machine learning identified key light absorbing organic compounds (details in Table S2 in the supplement)